Journal of Fluids and Structures (1993) **7**, 719–750

CHAOTIC DYNAMICS OF ARTICULATED CYLINDERS IN CONFINED AXIAL FLOW†

M. P. PAÏDOUSSIS AND R. M. BOTEZ
Department of Mechanical Engineering, McGill University, Montréal, Québec, H3A 2K6, Canada

(Received 30 June 1992 and in revised form 18 January 1993)

A study is presented of the dynamics of an articulated system of cylinders in confined axial flow. The articulated system is composed of rigid cylindrical segments, interconnected by rotational springs; it is cantilevered, hanging vertically in the centre of a cylindrical pipe, with fluid flowing downwards in the narrow annular passage. For sufficiently high flow velocity, the system generally loses stability sequentially by divergence (pitchfork bifurcation) and flutter (Hopf bifurcation). Once this occurs, the articulated system interacts with the outer pipe, which acts as a constraint to free motions. In the present study, which is mainly concerned with possible chaotic motions in this system, the analytical model is highly simplified. Thus, motions are considered to be planar, and the equations of the articulated system are taken to be linear, other than the terms associated with interaction with the outer pipe, which is modelled by either a trilinear or a cubic spring. A linear eigenvalue analysis is first undertaken, and then the nonlinear behaviour of the constrained model is explored numerically for systems of two and three articulations. Phase-plane plots, power spectral densities and bifurcation diagrams indicate in some cases a clear period-doubling cascade leading to chaos, while in others chaos arises via the quasiperiodic route. Poincaré maps and Lyapunov exponent calculations confirm the existence of chaos. Some analytical work is also presented, involving centre manifold theory, in which the post-Hopf limit-cycle amplitude is calculated and compared with that obtained numerically.

1. INTRODUCTION

EARLY INTEREST IN THE DYNAMICS of cylindrical structures in axial flow was related to (i) the small-amplitude turbulence-induced vibrations of fuel elements in nuclear reactors (Païdoussis 1966a; Reavis 1969; Gorman 1971) and (ii) the stability of the towed, sausage-like Dracone containers utilized for the transport of oil and fresh water by sea (Hawthorne 1961). Definitive studies of the stability of such systems, by means of linear theory, were undertaken by Païdoussis (1966b,c, 1968, 1973) and Dowling (1988a,b).

The dynamical behaviour of systems with both ends supported and cantilevered ones terminated by a streamlined end is similar: augmented, flow-induced damping at low flow velocities, and flow-induced instabilities at sufficiently high flows. Typically, stability is lost by *divergence*, and then at higher flow velocity by *flutter*: coupled-mode flutter in the case of cylinders with both ends supported and single-mode (Hopf) flutter in the case of cantilevered ones (Païdoussis 1966b,c, 1973). It is of interest that the

† An earlier version of this paper has been presented at the *Third ASME/JSME/CSME/IMechE/IAHR International Symposium on Flow-Induced Vibration and Noise*, Anaheim, CA, November 1992.

0889–9746/93/070719 + 32 $08.00

post-divergence flutter predicted by linear theory *does* in fact occur (Païdoussis 1966c) and is in good agreement with theoretical predictions. The behaviour of towed systems is considerably more complex, and rigid-body-type flow-induced instabilities are also possible (Païdoussis 1968; Dowling, 1988a,b).

Interest in *articulated* cylindrical systems in axial flow is a little more recent: (i) in conjunction with the dynamics of fuel "strings" or "stringers" of certain types of nuclear reactors (Païdoussis 1976), and (ii) underwater systems towed by a submarine (Hamy 1971; Païdoussis 1968, 1986). The fuel strings in question consist of fuel bundles held together by a central support tube; the string is mounted vertically within a pressure tube, and is held at the bottom end and free on top, with the flow upwards. The theoretical study by Païdoussis (1976) is of special interest here, since the physical system is quite similar to that considered in this paper, and hence so are the equations of motion—although in the case of the fuel string they are considerably more complex. Also of interest to the present study is the work on so-called "pendular oscillations" of articulated systems modelling nuclear reactor reactivity-monitoring or -control systems, e.g. by Hennig *et al.* (1980) and Peterka (1991), where the cylindrical elements are hung in the form of simple or compound pendula within a tube and are cooled by annular flow.

The present paper deals with the dynamics of a system of the type shown in Figure 1(a): an articulated system of cylinders interconnected by rotational springs, within a pipe containing flowing fluid. The annular space between the articulated system and the pipe is sufficiently narrow for impact to occur once motions become amplified, thus superimposing a strongly nonlinear element on the fluid-structure interaction problem. The dynamical behaviour of the system is studied with particular emphasis on chaotic dynamics; to this end, a number of idealizations are made to facilitate analysis, as will be explained in what follows.

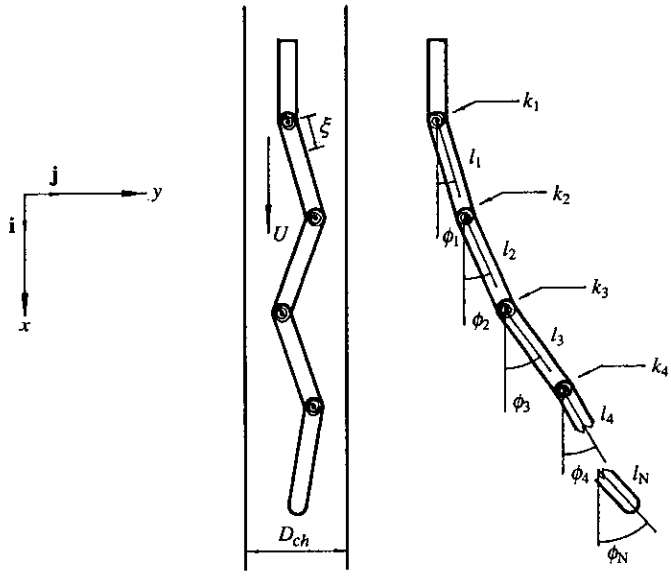

Figure 1. (a) Diagram of the articulated cylindrical system in confining channel, subjected to a mean annular flow velocity, U; (b) definition diagram for the generalized coordinates ϕ_j, $j = 1, \ldots, N$, showing the cylinder lengths, l_j, and interconnecting springs of stiffnesses k_j.

2. MATHEMATICAL FORMULATION

2.1. The Physical System and Assumptions Made

The articulated system here under consideration consists of a number of rigid cylinders interconnected by rotational springs, with the lowest cylinder being terminated by a more or less streamlined, ogival end. The system is hung vertically in the centre of a pipe [Figure 1(a)], and is supported at the upper end and free at the lower one. Fluid flows downward in the relatively narrow annular space.

To simplify the analytical model and thus to be able to carry out the analysis into the chaotic dynamics of the system easily, a number of assumptions are made at the outset, as follows: (i) motions of the articulated system are considered to be planar; (ii) the dynamics of the system when no impact occurs with the confining pipe are described by a linearized set of equations; (iii) impacting with the pipe is modelled by a trilinear or a cubic spring, presumed to exist between the pipe and the element of the articulated system contacting it. Assumption (i) is strictly simplifying: since the system under consideration does not model any particular physical system, it may be considered to be so constructed that motions are indeed planar. Assumption (ii) is justified by the narrowness of the annular gap [despite the diagrammatic spaciousness of Figure 1(a)]; thus, motions can only be of small amplitude, as constrained by the pipe. The presence of the pipe becomes "felt" by the system—quite apart from the effects on the fluid/flow-induced forces—via the impact-related forces. A trilinear model for such impact is quite reasonable: there is no spring (zero stiffness) while the system oscillates without touching the wall; but once it does, then further movement is resisted by a very large stiffness associated with local deformation of the articulated system and of the constraining pipe wall. The cubic spring is a further idealization of the situation (cf. Païdoussis & Moon 1988; Païdoussis *et al.* 1992), introduced strictly for analytical convenience.

Another assumption made implicitly is that, despite the articulations and the rotational springs (which are presumed not to protrude into the fluid flow), there is no local separation of the flow as the articulated system oscillates, by virtue of the small angles of deflection involved. For the same reason, slender-body theory will be presumed to be applicable for the determination of the inviscid fluid forces.

Concerning the fluid forces, they could, in principle, be determined by an appropriate solution of the Navier–Stokes equations. This will not be attempted here, and the fluid forces will be determined essentially by superposition: inviscid and viscous forces will be determined separately. This has been shown to be quite acceptable (Païdoussis 1966b,c, 1973) for the continuously flexible counterpart of the present problem, as well as for more complex systems (Païdoussis 1979). The equations of motion will be obtained by application of Lagrange's equations, for a system with an arbitrary number of articulations, N, although the calculations to be presented will be confined to $N = 2$ and $N = 3$. The generalized coordinates chosen are the angles ϕ_i, as shown in Figure 1(b).

2.2. The Structural Model

In this section, the kinetic and potential energies of the structure, i.e. of the articulated system itself, are determined. Small displacements have been assumed, so that $\sin \phi_j \simeq \phi_j$ and $\cos \phi_j \simeq 1$.

The local coordinate, ξ, is defined, along the length of each cylinder segment,

$0 \leq \xi \leq l_j$; then, for small deflections, the velocity at point ξ of the jth cylinder is

$$v_j(\xi) = \sum_{q=0}^{j-1} l_q \dot{\phi}_q + \xi \dot{\phi}_j, \tag{1}$$

where $\phi_0 = 0$ has been introduced for convenience and the dot denotes differentiation with respect to time, t. Hence, the kinetic energy of the jth cylinder is

$$T_{sj} = \frac{1}{2} \int_0^{l_j} m_j \left(\sum_{q=0}^{j-1} l_q \dot{\phi}_q + \xi \dot{\phi}_j \right)^2 \mathrm{d}\xi, \tag{2}$$

where m_j is the mass per unit length and the subscript s stands for "structural". The total kinetic energy of the structure, neglecting the ogival part of the last cylinder, is

$$T_s = \frac{1}{2} \sum_{j=1}^{N} \left[\int_0^{l_j} m_j \left(\sum_{q=0}^{j-1} l_q \dot{\phi}_q + \xi \dot{\phi}_j \right)^2 \right] \mathrm{d}\xi. \tag{3}$$

The potential energy is composed of a gravity component and a component due to strain of the intercylinder connecting springs. Again, for small displacements, it may easily be found to be

$$V_s = \frac{1}{2} \sum_{j=1}^{N} \left\{ \int_0^{l_j} m_j g \left(\sum_{q=0}^{j-1} l_q \phi_q^2 + \xi \phi_j^2 \right) \mathrm{d}\xi \right\} + \frac{1}{2} \sum_{j=1}^{N} k_j (\phi_j - \phi_{j-1})^2. \tag{4}$$

2.3. The Fluid-Dynamic Forces

As has already been mentioned, the fluid forces will be determined in several parts: inviscid unsteady forces, hydrostatic forces and viscous forces. They will generally be expressed as generalized forces for introduction into Lagrange's equations.

An element δx of one of the cylinders is shown in Figure 2, in which F_A represents the inviscid forces, F_{px} and F_{py} are the components of the hydrostatic pressure force,

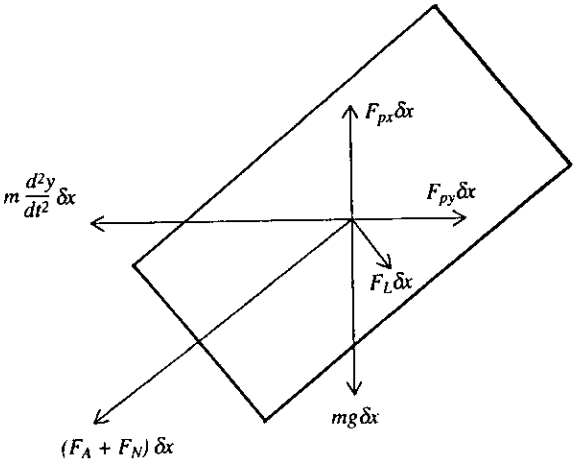

Figure 2. Forces acting on an element δx of one of the rigid cylinders of the articulated system.

and F_N and F_L are the normal and longitudinal viscous hydrodynamic forces, all per unit length.

2.3.1. *The inviscid hydrodynamic forces*

Using the system of coordinates with **i** and **j** unit vectors (Figure 1) and Lighthill's (1960) slender-body theory, the normal flow velocity at any point of a flexible cylinder is

$$\mathbf{v}(\xi) = U\mathbf{i} + [(\partial y/\partial t) + U(\partial y/\partial x)]\mathbf{j}. \tag{5}$$

Hence, for the jth (rigid) cylinder in the articulated system this leads to

$$\mathbf{v}_j(\xi) = U\mathbf{i} + \left(\sum_{q=1}^{j-1} l_q\dot{\phi}_q + \xi\dot{\phi}_j + U\phi_j\right)\mathbf{j}. \tag{6}$$

Therefore, the total kinetic energy of fluid, T_f, is

$$T_f = \frac{1}{2}\sum_{j=1}^{N}\left\{\int_0^{l_j}\left[M_{jn}\left(\sum_{q=1}^{j-1} l_q\dot{\phi}_q + \xi\dot{\phi}_j + U\phi_j\right)^2 + M_{jl}U^2\right]\right\}, \tag{7}$$

where $M_{jn} = \chi\rho A_j$ is the virtual or added mass of the jth cylinder subjected to transverse motions in the confined annular space, and M_{jl} is the equivalent quantity for axial motions. The added mass coefficient, χ, for axisymmetrically confined flow, is found by potential flow theory to be

$$\chi = [(1+h)^2 + 1]/[(1+h)^2 - 1], \tag{8}$$

where $h = D_h/D$, D being the diameter of the articulated cylinders, and $D_h = D_{ch} - D$ is the hydraulic diameter; D_{ch} is the internal diameter of the external pipe [Figure 1(a)].

If both ends of the articulated system were supported, expression (7) would represent the whole of the inviscid component of the fluid-dynamic forces. However, the cantilevered system is generally nonconservative, and hence there will generally be work done at the free end of the system by a nonconservative inviscid force, F_{nc} (cf. Benjamin 1961; Païdoussis 1966b). This force is associated with the non-cylindrical, ogival end of the last cylinder. For a less-than-ideally streamlined shape, this force (or force deficit, if one likes) arises because (i) the lateral flow will not be truly two-dimensional and (ii) boundary layer effects; for a flexible cylinder (Païdoussis 1966b), $F_{nc} = (1-f)MU[(\partial y/\partial t) + U(\partial y/\partial x)]$, in which f is a measure of departure from ideal slender-body flow theory: for an ideally streamlined end, $f \to 1$. This expression is adapted to the system at hand to give

$$F_{nc} = (1-f)M_N U\left(\sum_{j=1}^{N} l_j\dot{\phi}_j + U\phi_N\right). \tag{9}$$

2.3.2. *The hydrostatic pressure forces, F_{px} and F_{py}*

The static pressure distribution, $p(x)$, in the relatively narrow channel flow is determined by the hydrostatic pressure distribution, modified by the skin-friction-related pressure drop; since the latter is approximately linear, $p(x)$ is taken to be linear. The forces F_{px} and F_{py} acting on an element, $\delta\xi$, of one of the cylinders (Figure 2) are determined by considering this element frozen and immersed in fluid on all sides. Therefore, the resultant of the forces on the cylindrical surface of the jth cylinder (in terms of F_{px} and F_{py}) is equal to the total hydrostatic force on the element, which is the

buoyancy force, minus the forces pA acting on the cut, circular faces of the element; i.e.,

$$-F_{px}\,\delta\xi\mathbf{i} + F_{py}\,\delta\xi\mathbf{j} = -\frac{\mathrm{d}p}{\mathrm{d}x}A\,\delta\xi\mathbf{i} - \left(-\frac{\mathrm{d}(pA)}{\mathrm{d}x}\cos\phi_j\mathbf{i} - \frac{\mathrm{d}(pA)}{\mathrm{d}x}\sin\phi_j\mathbf{j}\right)\delta x, \qquad (10)$$

where $A\,\delta\xi$ is the elemental volume. Since, for the inclined cylinder, $\partial\xi/\partial x = \cos\phi_j$, the forces on the element $\delta\xi$ of the jth cylinder are

$$(F_{px})_j = 0, \quad (F_{py})_j = A\frac{\mathrm{d}p}{\mathrm{d}x}\tan\phi_j. \qquad (11)$$

These results could have been obtained directly from adaptation of the equivalent results for a flexible cylinder (Païdoussis, 1973): $F_{px} = 0$, $F_{py} = (\partial/\partial x)[pA(\partial y/\partial x)]$. From the latter, however, it is seen that there is also a change-of-angle (curvature term), which arises at the joints of the articulated cylinders. This gives rise to a contribution in the generalized force

$$(Q_p)_j = -(\mathrm{d}p/\mathrm{d}x)Al_i l_j \sin(\phi_i - \phi_j)$$

for the jth cylinder.

Moreover, by assuming that lateral movement of the cylinder has negligible effect on the axial pressure distribution, one may write

$$A\left(\frac{\mathrm{d}p}{\mathrm{d}x}\right) = -\left(\tfrac{1}{2}\rho DU^2 C_j \frac{D}{D_h}\right) + \rho gA, \qquad (12)$$

where $D_h = D_{ch} - D$ is the hydraulic diameter and C_f is the frictional coefficient. Hence, for small displacements ($\tan\phi_j \simeq \phi_j$) one obtains

$$(F_{py})_j = \left(-\tfrac{1}{2}\rho DU^2 C_f \frac{D}{D_h} + \rho gA\right)\phi_j. \qquad (13)$$

2.3.3. *Viscous hydrodynamic forces F_N and F_L*

The viscous forces acting on long inclined cylinders have been discussed by Taylor (1952). One can write these forces as follows:

$$F_N = \tfrac{1}{2}\rho DU^2(C_{dp}\sin^2\theta + C_f\sin\theta), \qquad F_L = \tfrac{1}{2}\rho DU^2 C_f\cos\theta, \qquad (14)$$

where $\theta = \tan^{-1}[(\partial y/\partial x)] + \tan^{-1}[(\partial y/\partial t)/U]$. For small $\partial y/\partial x$ and $(\partial y)/\partial t)/U$ these equations reduce to

$$F_N = \tfrac{1}{2}\rho DUC_f\left(U\frac{\partial y}{\partial x} + \frac{\partial y}{\partial t}\right) + \tfrac{1}{2}\rho DC_d\frac{\partial y}{\partial t}, \qquad F_L = \tfrac{1}{2}\rho DU^2 C_f, \qquad (15)$$

where the second term in F_N represents a linearization of the quadratic viscous force at zero flow velocity, $\tfrac{1}{2}\rho DC_{dp}\,|\partial y/\partial t|\,(\partial y/\partial t)$, in which the drag coefficient represents

$C_d = C_{dp}\overline{(\partial y/\partial t)}$. For a point in the jth cylinder these expressions may be written in the form

$$(F_N)_j = \tfrac{1}{2}\rho DUC_f\Big(\sum_{q=0}^{j-1} l_q\dot{\phi}_q + \xi\dot{\phi}_j + U\phi_j\Big) + \tfrac{1}{2}\rho DC_d\Big(\sum_{q=0}^{j-1} l_q\dot{\phi}_q + \xi\dot{\phi}_j\Big),$$
$$(F_L)_j = \tfrac{1}{2}\rho DU^2C_f. \tag{16}$$

One could have used the more sophisticated but complex theory of Mateescu & Païdoussis (1987) to obtain more accurate expressions for the unsteady components of $(F_N)_j$ and $(F_L)_j$—but, as shown by Païdoussis *et al.* (1990), the two sets of expressions give very similar results insofar as stability of the continuously flexible version of this system is concerned. Hence, the added complexity of that theory is not warranted for the purposes of this paper.

3. THE EQUATIONS OF SMALL MOTIONS

3.1. Kinetic and Potential Energies and Generalized Forces of the System

The total kinetic energy of the system, T, is given by

$$T = T_s + T_f, \tag{17}$$

where T_s and T_f are given by equations (3) and (7), respectively. The potential energy is exclusively associated with the articulated system, and so it is given by equation (4).

The generalized forces (actually moments) Q_j, $j = 1, 2, \ldots, N$, may be determined by considering the virtual work, δW_j, associated with virtual displacements, $\delta\phi_j$, in the generalized coordinates ϕ_j. Then the generalized force, Q_j, is defined via $\delta W_j = Q_j\,\delta\phi_j$. We proceed to determine the component of the generalized force Q_1, associated with cylinder 1 and denoted by $Q_{1,1}$. The corresponding virtual work, $\delta W_{1,1}$, is given by

$$\delta W_{1,1} = -\int_0^{l_1} (F_N)_1\xi\,\delta\phi_1\,\mathrm{d}\xi + \int_0^{l_1} (F_{py})_1\xi\,\delta\phi_1\cos\phi_1\,\mathrm{d}\xi, \tag{18}$$

from which $Q_{1,1} = \delta W_{1,1}/\delta\phi_1$.

Similarly, the virtual work associated with the forces acting on the second cylinder, $\delta W_{1,2}$, due to a virtual displacement associated with the generalized coordinate ϕ_1, is given by

$$\delta W_{1,2} = -\int_0^{l_2} 0\,(F_N)_2 l_1\,\delta\phi_1\cos(\phi_2-\phi_1)\,\mathrm{d}\xi + \int_0^{l_2} (F_{py})_2 l_1\,\delta\phi_1\cos\phi_1\,\mathrm{d}\xi$$
$$+ \int_0^{l_2} (F_L)_2 l_1\,\delta\phi_1\sin(\phi_2-\phi_1)\,\mathrm{d}\xi - (\mathrm{d}p/\mathrm{d}x)_2 A_2 l_2 l_1\,\delta\phi_1\sin(\phi_2-\phi_1); \tag{19}$$

and so on for $\delta W_{1,k}$, $k = 3, \ldots, N-1$, from which the $Q_{1,k}$ may be determined. The virtual work associated with the last cylinder, $\delta W_{1,N}$, will have the additional terms

$$\tfrac{1}{2}\rho D^2U^2C_b l_1\,\delta\phi_1\sin(\phi_N-\phi_1) - F_{nc}l_1\,\delta\phi_1\cos(\phi_N-\phi_1), \tag{20}$$

where C_b is the base drag coefficient, and F_{nc} has been discussed in Section 2.3.1. The

total generalized force is simply given by

$$Q_1 = \sum_{j=1}^{N} Q_{1,j}.$$

Proceeding in this manner and linearizing, the generalized force associated with the generalized coordinate ϕ_j is

$$\begin{aligned} Q_j = &- \int_0^{l_j} (F_N)_j \xi \, d\xi + \int_0^{l_j} (F_{py})_j \xi \, d\xi + \sum_{i=j+1}^{N} \left\{ - \int_0^{l_i} (F_N)_i l_j \, d\xi + \int_0^{l_i} (F_{py})_i l_j \, d\xi \right. \\ &\left. + \int_0^{l_i} (F_L)_i l_j (\phi_i - \phi_j) \, d\xi - (dp/dx)_i A_i l_i l_j (\phi_i - \phi_j) \right\} \\ &+ \tfrac{1}{2}\rho D^2 U^2 C_b l_j (\phi_N - \phi_j) - F_{nc} l_j, \end{aligned} \tag{21}$$

where $(F_N)_j$ and $(F_L)_j$, $(F_{py})_j$, F_{nc} are given by linearized versions of equations (16), (13) and (9), respectively, for small amplitudes ϕ_j (such that $\sin \phi_j \simeq \phi_j$, $\cos \phi_j \simeq 1$), and the change-of-angle (curvature) term of Section 2.3.2 has also been included.

3.2. Derivation of the Linearized Equations of Motion

Equations (3), (4), (7) and (21) are substituted into Lagrange's equations,

$$\frac{d}{dt}\left(\frac{\partial T}{\partial \dot{\phi}_j}\right) - \frac{\partial T}{\partial \phi_j} + \frac{\partial V}{\partial \phi_j} = Q_j, \qquad j = 1, 2, \ldots, N, \tag{22}$$

for a system of N articulations, yielding N linear equations of the form

$$F_j(\ddot{\phi}_1, \ldots, \ddot{\phi}_N; \dot{\phi}_1, \ldots, \dot{\phi}_N; \phi_1, \ldots, \phi_N) = 0, \qquad j = 1, 2, \ldots, N. \tag{23}$$

The equations obtained up to this point are valid, only provided that motions are sufficiently small for impact with the outer pipe not to occur; the nonlinear forces generated by impact will be introduced later (Section 5).

We next consider a "uniform" system, where all the articulations have the same mass per unit length ($m_j = m$, $j = 1, \ldots, N$) and physical dimensions ($A_j = A$, $D_j = D$, etc., $j = 1, \ldots, N$), including length $l_j = l$, $j = 1, \ldots, N-1$, except for the last articulation, which is l_N long (see next paragraph). Similarly, the stiffnesses of all intercylinder springs are equal, $k_j = k$, $j = 1, \ldots, N$.

The equations of motion may now be rendered non-dimensional with the aid of the dimensionless parameters

$$\begin{gathered} \beta = \rho A/(\rho A + m), \qquad \gamma = (m - \rho A) g L^2 N/k, \qquad u = (\rho A L N/k)^{1/2} U, \\ \varepsilon = L/D, \qquad l_N = \varepsilon l, \qquad c = (4/\pi) C_d [MLN/k]^{1/2}, \qquad c_f = (4/\pi) C_f, \\ c_b = (4/\pi) C_b, \qquad h = D_h/D, \qquad \tau = [(\rho A + m) L^3 N/k]^{-1/2} t, \end{gathered} \tag{24}$$

where $L = Nl$, and k is taken to be $k = EI/l$, EI being the flexural rigidity of a fictitious, continuously flexible system to which the present system would converge as $N \to \infty$ (Païdoussis & Deksnis 1970). In a study of convergence of an articulated system of

pipes conveying fluid (discrete N) to the equivalent continuously flexible one ($N = \infty$) as N is increased, it was found (Païdoussis & Deksnis 1970) that optimum convergence is achieved with the length of the last articulation $l_N = el$, $e = \frac{1}{2}$; this value is arbitrarily adopted here also.

The equations of motion have been obtained for a system of N articulations; however, the results to be discussed in this paper are confined to $N = 2$ and $N = 3$. The nondimensional equations for a two-degree-of-freedom system ($N = 2$) are the following:

$$
\begin{aligned}
&[1 + (\chi - 1)\beta][(\tfrac{1}{3} + e)\ddot{\phi}_1 + \tfrac{1}{2}e^2\ddot{\phi}_2] + \tfrac{1}{6}(3e + 1)\varepsilon c_f u\sqrt{\beta}\dot{\phi}_1 + \tfrac{1}{6}(3e + 1)\varepsilon c\sqrt{\beta}\dot{\phi}_1 \\
&+ \chi(1 - f)uN\sqrt{\beta}\dot{\phi}_1 + \tfrac{1}{4}\varepsilon c_f e^2 u\sqrt{\beta}\dot{\phi}_2 + \tfrac{1}{4}\varepsilon c\sqrt{\beta}e^2\dot{\phi}_2 \\
&+ \chi(2 - f)uNe\sqrt{\beta}\dot{\phi}_2 - \chi u^2N^2\phi_1 + N^4\phi_1 + N\gamma\frac{1 + 2e}{2}\phi_1 - N^4(\phi_2 - \phi_1) \\
&+ \tfrac{1}{4}(1 + h^{-1})(2e + 1)u^2N\varepsilon c_f\phi_1 + \tfrac{1}{2}u^2N^2c_b(\phi_1 - \phi_2) + \chi(1 - f)u^2N^2\phi_2 = 0, \qquad (25) \\
&[1 + (\chi - 1)\beta][\tfrac{1}{2}e^2\ddot{\phi}_1 + \tfrac{1}{3}e^3\ddot{\phi}_2] + \tfrac{1}{4}e^2\sqrt{\beta}u\varepsilon c_f\dot{\phi}_1 + \tfrac{1}{4}e^2\sqrt{\beta}\varepsilon c\dot{\phi}_1 - \chi uNef\sqrt{\beta}\dot{\phi}_1 \\
&+ \tfrac{1}{6}e^3\sqrt{\beta}u\varepsilon c_f\dot{\phi}_2 + \tfrac{1}{6}e^3\sqrt{\beta}\varepsilon c\dot{\phi}_2 + \chi(1 - f)uNe^2\sqrt{\beta}\dot{\phi}_2 + N^4(\phi_2 - \phi_1) \\
&+ \tfrac{1}{2}e^2N\gamma\phi_2 + \tfrac{1}{4}e^2(1 + h^{-1})u^2N\varepsilon c_f\phi_2 - \chi u^2N^2ef\phi_2 = 0,
\end{aligned}
$$

where the dots now denote differentiation with respect to τ. [It is noted that the definition of h in equations (24) is the inverse of what it is in some previous work (e.g., Païdoussis 1973); hence, the terms $1 + h^{-1}$ here correspond to $1 + h$ therein. The present definition is physically more meaningful: a small h represents a narrow annulus.]

The analysis that immediately follows, in Sections 4, 5 and 6, is exclusively confined to the two-degree-of-freedom ($N = 2$) version of the system. The three-degree-of-freedom system is considered in Section 7, where the equivalent of equations (25) for $N = 3$ are also given.

4. STABILITY ANALYSIS OF THE LINEARIZED SYSTEM ($N = 2$)

Before considering the full problem, involving impact of the articulated system with the outer channel, it is important to understand the small-amplitude dynamical behaviour, where such impact does not occur. This is provided by an eigenvalue analysis of the linearized equations (25). The dimensionless equations of motion are rewritten in matrix form,

$$[M]\{\ddot{\phi}\} + [C]\{\dot{\phi}\} + [K]\{\phi\} = [0]; \qquad (26)$$

solutions are then sought of the form

$$\{\phi\} = \{\bar{\phi}\}\exp(i\omega t), \qquad (27)$$

and they are obtained by transforming equation (26) into a first-order system and then solving it as a standard eigenvalue problem. The eigenvalues $\lambda_i \equiv i\omega_i$ of the system, which are generally complex, permit the assessment of stability for each set of system parameters.

Critical values of a parameter, in our case the flow velocity u, are needed in order to determine where the eigenvalues of the linearized system contain a purely imaginary pair (Hopf bifurcation) or a single zero value (pitchfork bifurcation).

The dynamical behaviour of the system of two articulations is investigated for the

following set of parameters:

$$\varepsilon = 10, \quad e = 0{\cdot}5, \quad f = 0{\cdot}8, \quad \beta = 0{\cdot}4, \quad \gamma = 10, \quad \varepsilon c_f = 0{\cdot}25, \quad c_b = 0{\cdot}1. \tag{28}$$

We choose two cases,

$$\begin{aligned} &\textit{Case 1; wider annulus:} \quad h = 0{\cdot}5, \quad \text{for which} \quad c = 0{\cdot}38 \ (C = 0{\cdot}30); \\ &\textit{Case 2; narrower annulus:} \quad h = 0{\cdot}2, \quad \text{for which} \quad c = 0{\cdot}79 \ (C = 0{\cdot}62). \end{aligned} \tag{29}$$

Figure 3 ($h = 0{\cdot}5$) and Figure 4 ($h = 0{\cdot}2$) show, in the form of Argand diagrams, the real and imaginary parts of the eigenvalues of the system, $\mathcal{R}e(\omega)$ and $\mathcal{I}m(\omega)$ for (a) the first and (b) the second mode of the system, as functions of the flow velocity.

As the flow velocity is increased in Figure 3, both the real and imaginary components of the first-mode eigenvalue approach zero; this corresponds to a divergence instability (pitchfork bifurcation), which occurs at $u = 1{\cdot}695$. As u is increased further, the real part of the eigenvalues again becomes negative, so that the system is restabilized, at

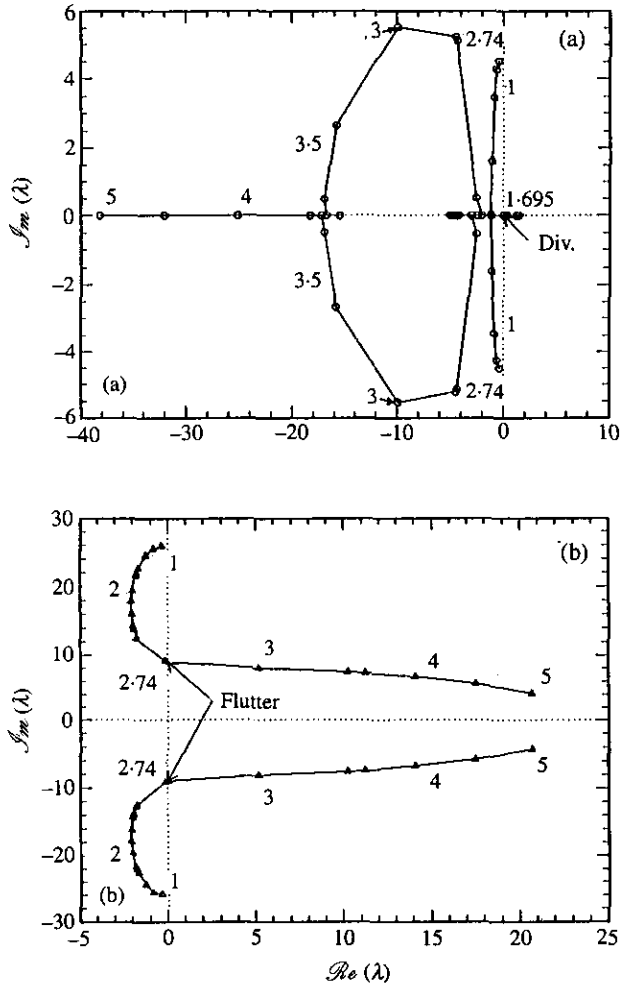

Figure 3. Argand diagrams for (a) the first mode and (b) the second mode of the system of Case 1 ($h = 0{\cdot}5$), as defined by (29) and for system parameters (28). The imaginary part of the eigenvalue, $\mathcal{I}m(\lambda)$, is plotted versus the real part, $\mathcal{R}e(\lambda)$, with the nondimensional flow velocity, u, as parameter.

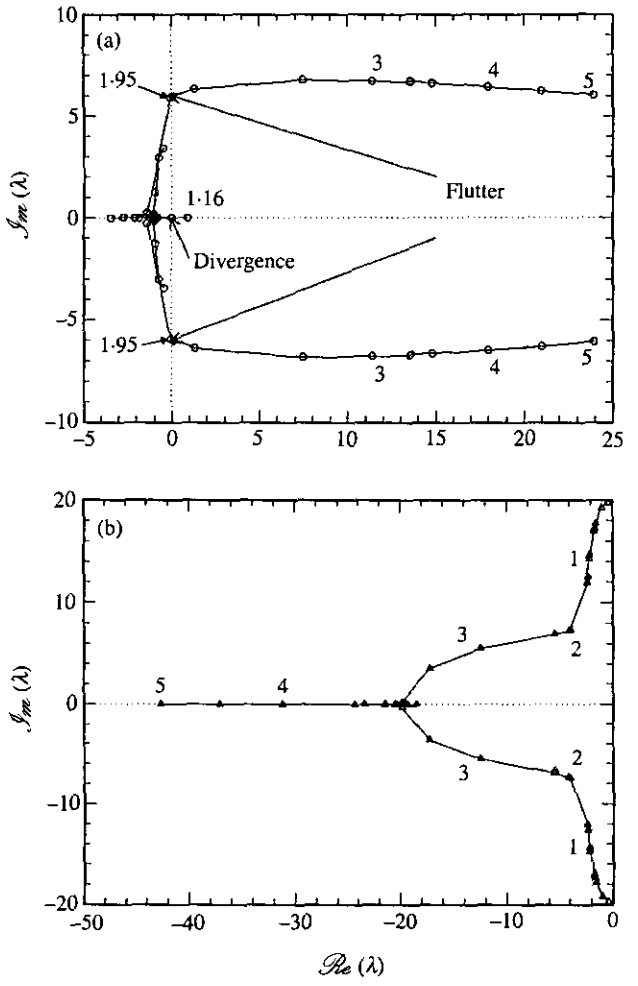

Figure 4. Argand diagrams for (a) the first and (b) the second mode of the system of Case 2 ($h = 0{\cdot}2$), as defined by (29) and (28); $\mathcal{I}_m(\lambda)$ is plotted versus $\mathcal{R}_e(\lambda)$, with the dimensionless flow velocity, u, as parameter.

$u = 2{\cdot}53$. Furthermore, at $u = 2{\cdot}74$, in the second mode, purely imaginary eigenvalues arise, which corresponds to a flutter instability (Hopf bifurcation). As u is increased beyond 2·74, the real part becomes positive and this corresponds to a linearly unstable system (amplified oscillations).

For the lower value of h (Figure 4), the real and imaginary parts of the first-mode eigenvalue vanish for $u = 1{\cdot}16$; this value of u corresponds to the pitchfork bifurcation. The system is restabilized between $u = 1{\cdot}71$ and $u = 1{\cdot}95$. Then, flutter (Hopf bifurcation) occurs at $u = 1{\cdot}95$ in the first mode. In the second mode, the real part of the eigenvalues is always negative; so, from the linear stability point of view, only the first-mode behaviour is of interest.

From the results presented here, it can be seen that, for the larger gap ($h = 0{\cdot}5$), larger critical flow velocities are obtained than for the smaller gap ($h = 0{\cdot}2$): $u = 1{\cdot}695$ and 2·74 *versus* $u = 1{\cdot}16$ and 1·95. This trend can further be verified by studying the behaviour of the system in unconfined flow; in that case, much higher critical flow velocities than those for confined flow are obtained.

5. NONLINEAR BEHAVIOUR, IMPACTING WITH THE CHANNEL WALL: NUMERICAL RESULTS $N = 2$

5.1. Trilinear and Cubic Spring Description

Following the onset of flutter instability, the amplitude of oscillation will grow, resulting in impacting with the outer cylinder. The interaction with the outer cylinder is approximately trilinear, as shown in Figure 5. For contact at the second articulation (lower end of the first cylinder)† and denoting the displacement at that point by $\eta = l_1\phi_1$ and the contact stiffness by k_t, the force exerted by the trilinear spring may be expressed as

$$F_t(\eta) = k_t\{\eta - \tfrac{1}{2}[|\eta + \eta_g| - |\eta - \eta_g|]\},$$

where η_g is defined in Figure 5. Recalling that in the equations of motion we are dealing with moments and angles, rather than forces and displacements, the nondimensional term associated with the trilinear spring that should be added to the first of equations (25) is

$$\mathcal{M}_t = \kappa_t\{\phi_1 - \tfrac{1}{2}[|\phi_1 + \phi_g| - |\phi_1 - \phi_g|]\}, \tag{30}$$

where $\phi_g = \eta_g/l_1$ (with $l_1 = l$, see Section 3.2), $\kappa_t = (k_t/k)L^2N^2$, and k is the rotational stiffness at one of the articulations (see Sections 2.2 and 3.2).

For analytical convenience, an alternative, cubic-spring approximation may be utilized instead to model impacting with the outer cylinder. The force-displacement relationship in this case is

$$F_c(\eta) = k_c\eta^3,$$

and the nondimensional term that must be added to the first of equations (25) is

$$\mathcal{M}_c = \kappa_c\phi_1^3, \tag{31}$$

where $\kappa_c = (k_c/k)L^4$.

Solutions of the equations of motion, with either (30) or (31) included, were

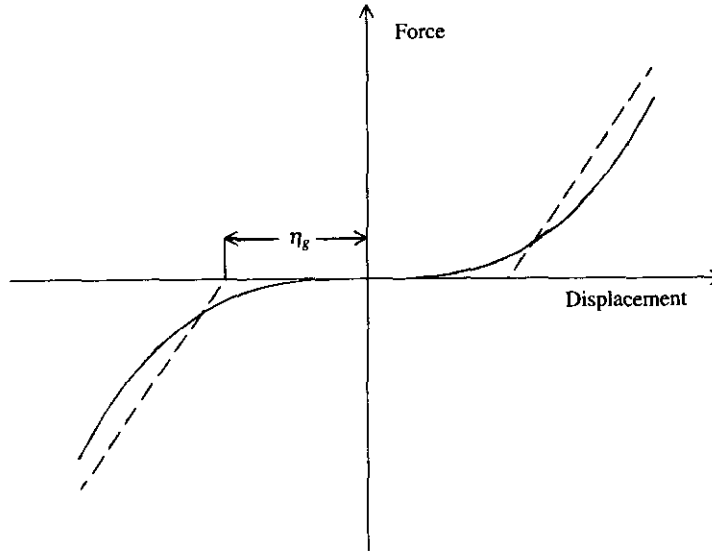

Figure 5. Force-displacement curves for the realistic trilinear-spring model (– – –) for impacting of the articulated system on the confining channel, and the cubic-spring idealization (——).

† This, in fact, was later confirmed to represent the 'natural' actual motion.

obtained by using a fourth-order Runge–Kutta integration algorithm, with a dimensionless time-step of $\Delta\tau = 0{\cdot}01$. The same two cases as in the linear analysis have been studied, Cases 1 and 2 of (29).

5.2. Bifurcation and Phase-plane-Diagrams

Graphing a typical property of the solution, e.g. the maximum displacement, ϕ_{max}, as a function of u, we construct the bifurcation diagram. To clarify its meaning, phase-plane portraits are also presented. In the results to be shown, ϕ_{max} corresponds to the maximum value of $\phi_1(t)$.

Figure 6 shows the bifurcation diagram with the trilinear spring representation for Case 1 of (29), i.e. for $h = 0{\cdot}5$ and $\kappa_t = 80$, and Figure 7 the bifurcation diagram with

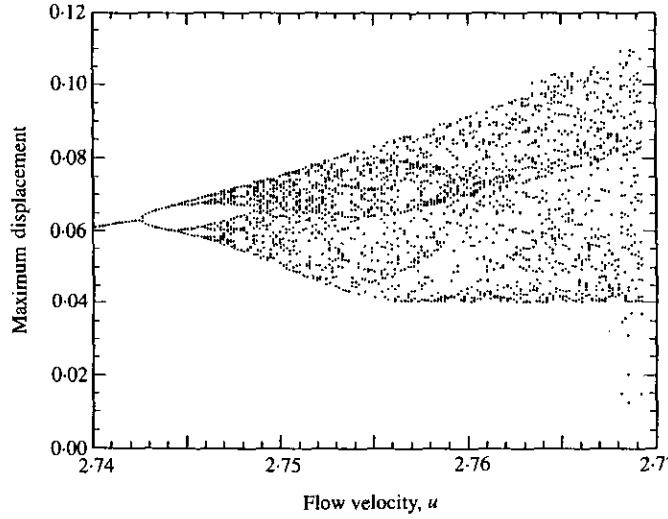

Figure 6. Bifurcation diagrams for the system with the wider annulus, $h = 0{\cdot}5$ [as defined by (28) and (29)] and $\kappa_t = 80$, showing ϕ_{1max} versus u, obtained with the trilinear-spring model for impacting with the channel.

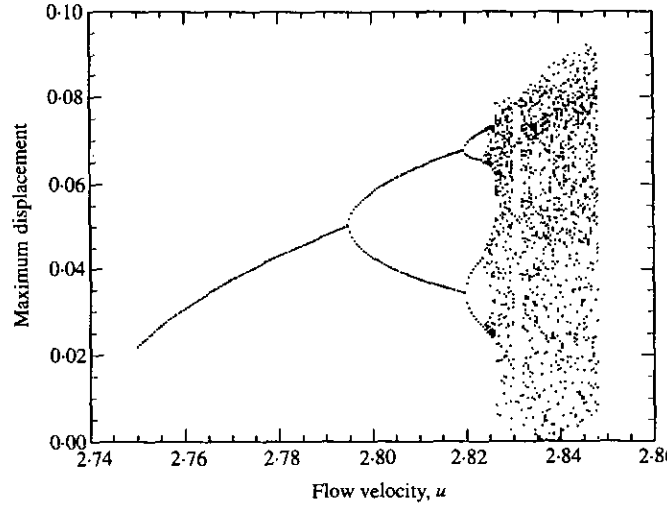

Figure 7. Bifurcation diagram for the same system as in Figure 6 ($h = 0{\cdot}5$), but with the cubic-spring model ($\kappa_c = 5 \times 10^3$) for impacting with the channel.

the cubic-spring representation ($\kappa_c = 5 \times 10^3$) for the same case. The range of u shown covers the behaviour beyond the Hopf bifurcation. It is seen that, qualitatively, the dynamical behaviour in the two cases is similar, and attention will henceforth be diverted to the more idealized system involving the cubic spring. The reason for this is that direct comparison with analytical work to be presented in Section 6 then becomes possible, because representation (31) is an analytical function, whereas (30) is not. Thus, concentrating on the cubic spring representation with $\kappa_c = 5 \times 10^3$, Figures 7–10 show bifurcation diagrams and phase-plane portraits for the first cylinder in the system, for flow velocities above the critical velocity for flutter.

The route to chaos for the bifurcation diagram of Figure 7 (Case 1, $h = 0{\cdot}5$) is clarified via the phase-plane portraits of Figure 8. For $u = 2{\cdot}74$, there exists a stable, symmetric limit cycle that develops after the Hopf bifurcation (not shown). The symmetry of the limit cycle is lost by a symmetry-breaking pitchfork bifurcation at $u = 2{\cdot}795$, the first bifurcation shown in Figure 7— where the two branches are obtained with different-sign initial conditions. At higher u, a cascade of period-doubling bifurcations occurs, and Figure 8(a, b) shows period-2 and period-4 motions. Figure 8(c) shows chaotic motion for $u = 2{\cdot}8295$, corresponding to the first dense cloud of points in the bifurcation diagram. Figure 8(d) shows a periodic (akin to period-5) motion for $u = 2{\cdot}831$, corresponding to the sparse patch (periodic window) in the bifurcation diagram. At higher u, the motion becomes strongly chaotic again.

The period-doubling bifurcations have been pin-pointed to occur at $u = 2{\cdot}8195$ (period-2), $u = 2{\cdot}8234$ (period-4), $u = 2{\cdot}8243$ (period-8) etc., where the interval in u

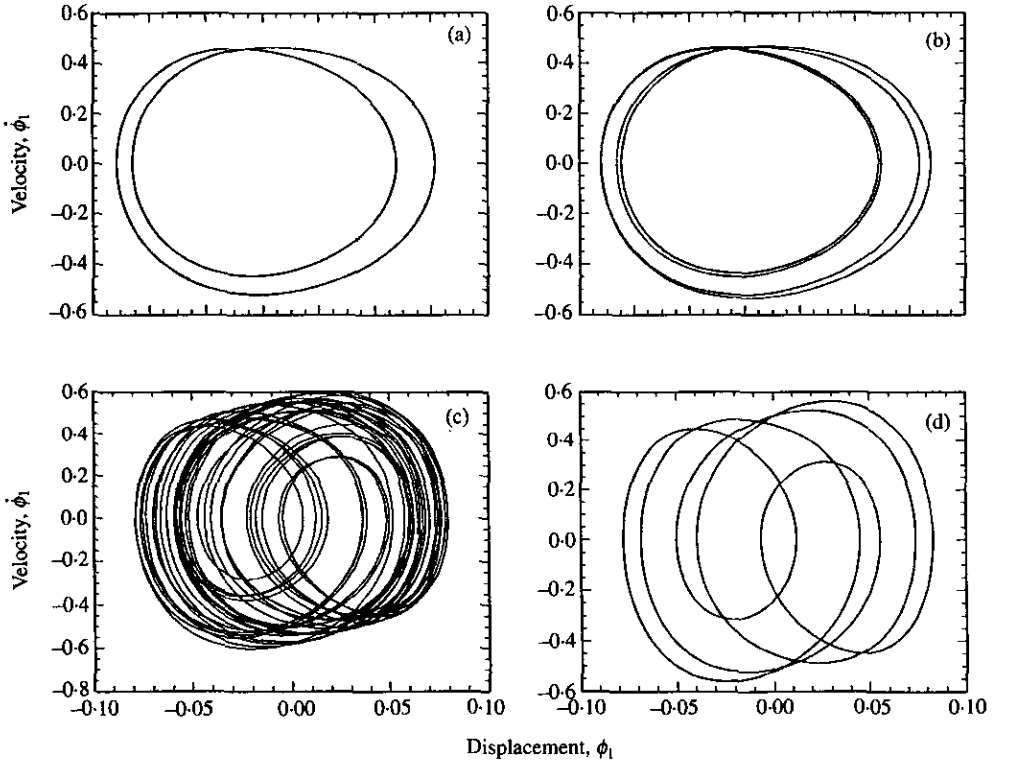

Figure 8. Phase-plane plots of $\dot{\phi}_1$ versus ϕ_1 at (a) $u = 2{\cdot}8225$, (b) $u = 2{\cdot}8240$, (c) $u = 28295$ and (d) $u = 2{\cdot}8310$, for the system of Figure 7.

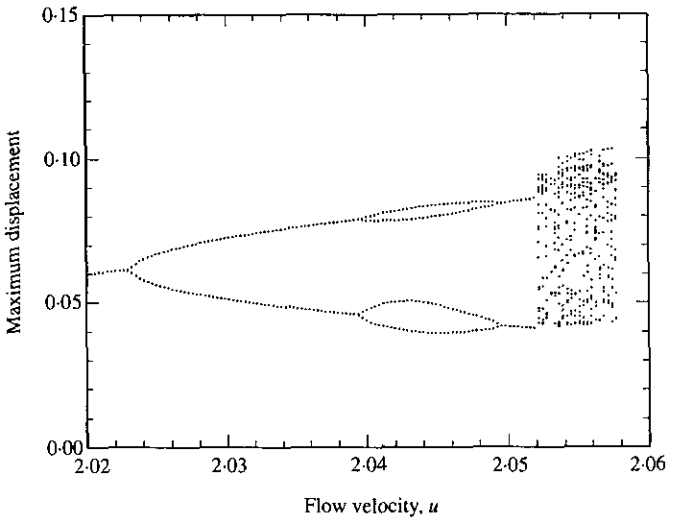

Figure 9. Bifurcation diagram for the system with the narrower annulus, $h = 0{\cdot}2$ [as defined by (28) and (29)], showing $\phi_{1\max}$ versus u, with the cubic spring model ($\kappa_c = 5 \times 10^3$).

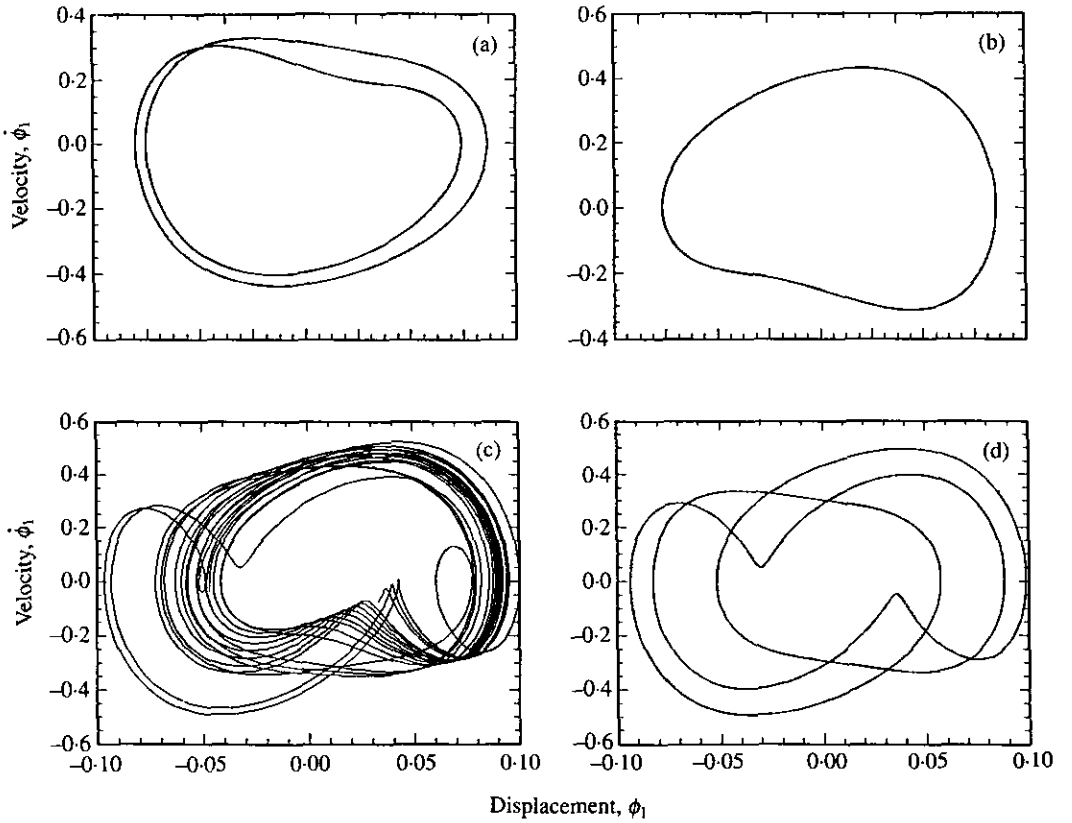

Figure 10. Phase-plane plots of $\dot{\phi}_1$ versus ϕ_1 at (a) $u = 2{\cdot}045$, (b) $u = 2{\cdot}050$, (c) $u = 2{\cdot}0535$ and (d) $u = 2{\cdot}0568$ for the system of Figure 9.

between bifurcations becomes progressively smaller. From these values, the Feigenbaum number, $\text{Fei}_j = (u_{j+1} - u_j)/(u_{j+2} - u_{j+1})$, may be computed, giving Fei = 4·33, which is reasonably close to the "ideal" Fei = 4·6692 (Moon 1987).

For the narrower annulus (Case 2, $h = 0{\cdot}2$), the dynamical behaviour is broadly similar, but quite different in detail, as seen in the bifurcation diagram (Figure 9) and phase-plane diagrams (Figure 10). The symmetry-breaking pitchfork bifurcation occurs at $u \simeq 2{\cdot}023$ (Figure 9). This is followed by a "period-bubbling" event, where a period-doubling bifurcation occurs but is then reversed to period-1 motion, in the interval $2{\cdot}0395 < u < 2{\cdot}0495$; period-2 and period-1 phase-plane portraits shown in Figure 10(a, b) for $u = 2{\cdot}045$ and 2·050, respectively. At $u = 2{\cdot}05225$ (Figure 9) the motion becomes quasiperiodic-2, but, if the calculation is carried out for sufficient nondimensional time steps (>100), it develops into chaotic motion. This occurs in the neighbourhood of $u = 2{\cdot}052$; for larger u the transition to chaos is much faster. A typical chaotic phase portrait is shown in Figure 10(c) for $u = 2{\cdot}0535$. Thus, this system follows the quasiperiodic route to chaos. Chaos persists to $u = 2{\cdot}058$, with a quasiperiodic window at $u = 2{\cdot}0568$ [Figure 10(d)], which looks like period-3 motion (see Section 5.3).

5.3. Power Spectra and Time Traces

The results obtained could be verified by constructing time traces and the corresponding power spectra for the displacement of the first cylinder. They are important, especially for the quasiperiodic motion.

Case 1 of (29), for $h = 0{\cdot}5$, involving a cascade of period-doubling bifurcations, is quite similar to that studied by Païdoussis & Moon (1988) and Païdoussis *et al.* (1991), for instance, for a similar problem. The chaotic character of the motion at $u = 2{\cdot}8295$ is self-evident in Figure 11(a), in both the PSD and the time trace. The motion depicted in Figure 11(b) for $u = 2{\cdot}831$ is periodic, with the dominant dimensionless frequency of $f = 2{\cdot}245$, modulated mainly by its fifth subharmonic of $f = 0{\cdot}449$; this gives rise to the period-5-like phase portrait of Figure 8(d). The second peak in the PSD corresponds to $f = \frac{3}{5} \times 2{\cdot}245$ and, indeed, Figure 8(d) could be considered as a "modified" form of period-3 motion also!

Finally, Figure 11(c) depicts quasiperiodic-2 motion, for Case 2 of (29) and $u = 2{\cdot}0568$, where the power spectrum was obtained from a 100 time-step trace. The two dominant frequencies are $f_1 = 0{\cdot}377\,5748$ and $f_2 = 1{\cdot}150\,704$, so that all other peaks in the PSD may be confirmed to correspond to $f = nf_1 \pm mf_2$, with n and m integers; for example, the third peak in the FFT is $2f_2 - f_1$, while the fourth is $2f_2 + f_1$. Thus, despite Figure 10(d) looking like period-3 motion, it represents more complex behaviour. The ratio f_1/f_2, usually referred to as the *winding* (or rotation) number, is $W = 0{\cdot}328\,125 = 21/64$, a rational number, as found by the continued fraction method by using *Mathematica* software. (Whether f_1/f_2 is truly rational and equal to 21/64, and hence the Poincaré map would have a *finite* number of points, depends on the accuracy of determination of f_1 and f_2 as given above.)

5.4. Poincaré Maps and Lyapunov Exponents

The Poincaré map gives a qualitative picture of the type of dynamical behaviour that occurs. Thus, when the solution is periodic (period-1), the phase-plane portrait is a limit cycle and the Poincaré map, which is a section through the limit cycle, is but a single point; when the dynamics is chaotic, the Poincaré map becomes more complex,

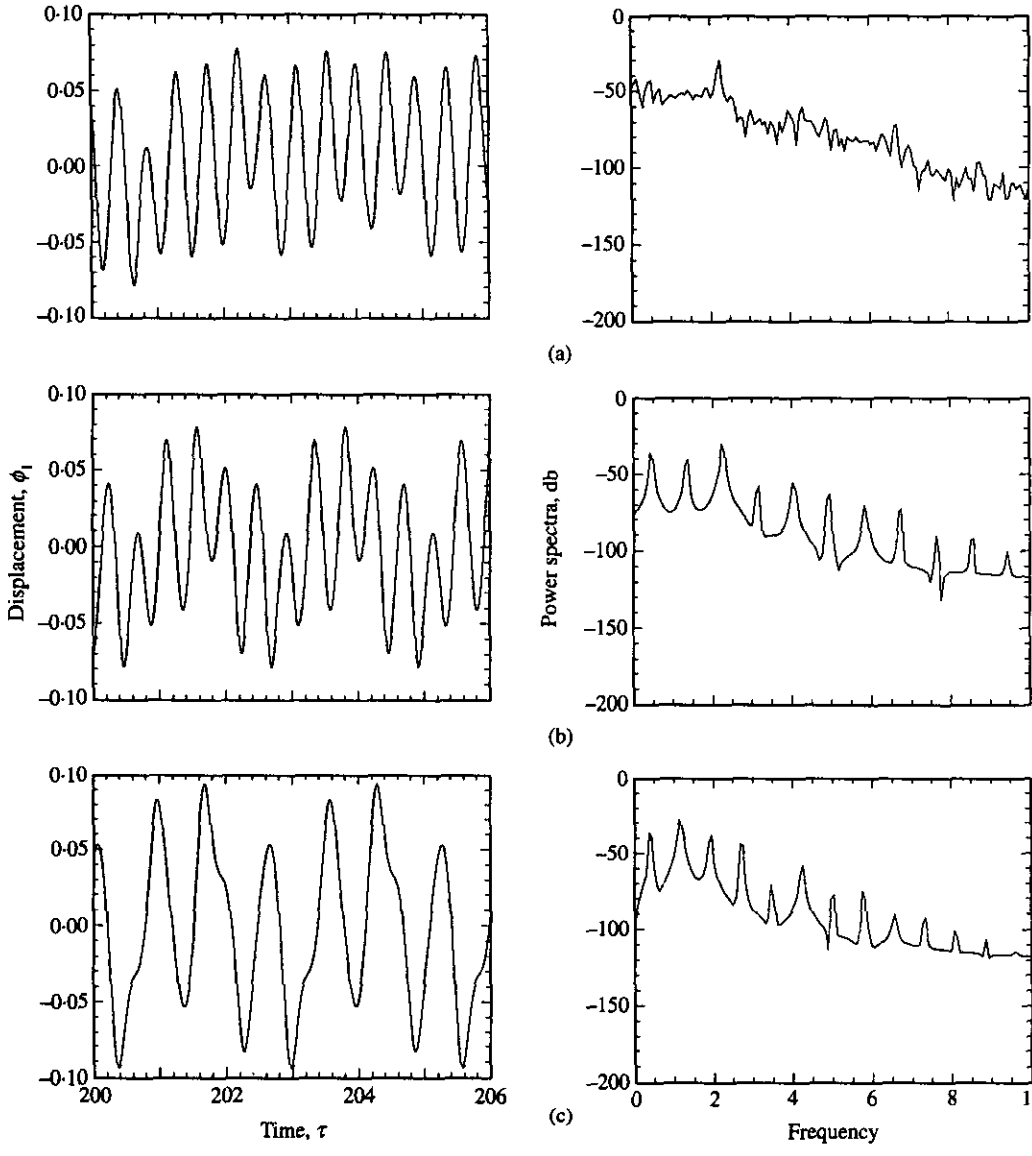

Figure 11. Time traces of $\phi_1(\tau)$ and power spectra (dB) plotted in dimensionless time, τ, and the corresponding dimensionless frequency, for (a, b) the system of Figure 7 ($h = 0{\cdot}5$, $u = 2{\cdot}8295$ and $2{\cdot}8310$) and (c) the system of Figure 9 ($h = 0{\cdot}2$, $u = 2{\cdot}0568$); (a), (b) and (c) show, respectively, chaotic, subharmonically modualted periodic and quasiperiodic motions.

but nevertheless should retain some definite structure, in contrast to that for a random process.

A plot of the largest Lyapunov exponent, σ, versus a parameter (here u) gives a *quantitative* assessment of the dynamical state: if $\sigma < 0$, this means the system will eventually return to a stable fixed point, i.e. the system is stable; if $\sigma = 0$ the motion is associated with a periodic or quasiperiodic solution, i.e. to a limit cycle; if $\sigma > 0$, the motion is chaotic. For the techniques and definitions involved the reader is referred to any book on chaos, e.g. by Moon (1987); see also Benettin *et al.* (1980).

The Poincaré maps have been obtained by plotting $\dot{\phi}_2$ versus ϕ_2 when $\phi_1 = 0$.

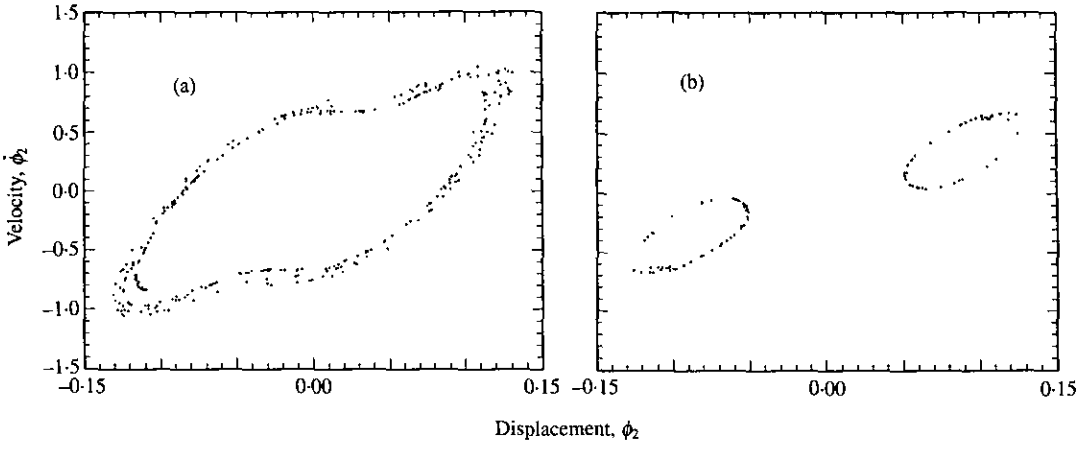

Figure 12. Poincaré maps of $\dot{\phi}_2(\tau)$ versus $\phi_2(\tau)$ when $\phi_1(\tau) = 0$ for (a) the wider-annulus system ($h = 0{\cdot}5$, $u = 2{\cdot}84$) in the chaotic region, and (b) the narrower-annulus system ($h = 0{\cdot}2$, $u = 2{\cdot}052525$) in quasiperiodic mode, just prior to the onset of chaos.

Figure 12(a), for Case 1 and $u = 2{\cdot}84$, shows a typical Poincaré map in the chaotic regime. A very definite structure is seen to exist, the map showing some similarity (in this cross-sectional form) to a Möbius strip (cf. Païdoussis *et al.* 1992). Figure 12(b), for Case 2 and $u = 2{\cdot}052525$, close to the onset of chaos, corresponds to quasiperiodic-2 motion that eventually becomes chaotic. In Figure 12(b) we see the closed curves characteristic of quasiperiodic motion, but with the beginnings of chaotic perturbations off the curves clearly visible.

The largest Lyapunov exponents shown in Figure 13 display basically similar behaviour for (a) $h = 0{\cdot}5$ (Case 1) and (b) $h = 0{\cdot}2$ (Case 2): beyond a certain threshold (cf. Figures 7 and 9), the motion is chaotic and remains so ($\sigma > 0$), apart from one region of periodic [Figure 13(a)] and quasiperiodic [Figure 13(b)] motion ($\sigma = 0$).

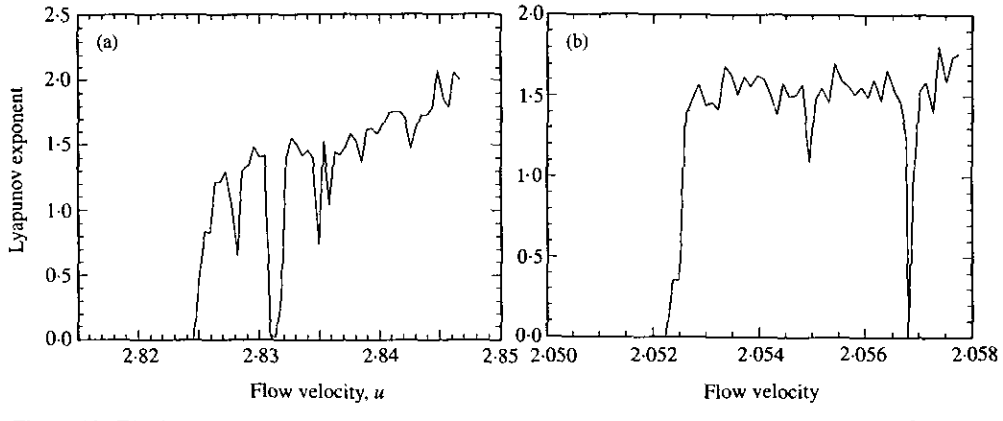

Figure 13. The largest Lyapunov exponent versus u for the (a) $h = 0{\cdot}5$ and (b) $h = 0{\cdot}2$ systems [defined by (28) and (29) and $\kappa_c = 5 \times 10^3$].

6. ANALYTICAL RESULTS: CENTRE MANIFOLD THEORY

Centre manifold theory is a method which uses power series expansions in the neighbourhood of an equilibrium point in order to reduce the dimension of a system of ordinary differential equations, thereby helping to understand the dynamical behaviour of an otherwise complex system.

At a degenerate point, which has at least some eigenvalues with zero real part, the space in which the system dynamics evolve can be divided into three subspaces: the stable, unstable and centre eigenspaces, spanned by the eigenvectors whose eigenvalues have negative, positive and zero real parts. At this degenerate point, there exist three invariant subspaces similarly called stable, unstable and centre manifolds, tangent to the corresponding linear counterparts at the fixed point. Since the stability properties of the dynamical system along the stable and unstable manifolds are known, the system dynamics in the vicinity of the degenerate point is completely determined by the flow restricted on the centre manifold.

6.1. Computation of the Unfolding Parameters

Our system of equations is written in the following form:

$$\dot{\mathbf{y}} = \mathbf{A}(u, \beta, \gamma)\mathbf{y} + \varepsilon \mathbf{f}(\mathbf{y}), \tag{32}$$

where $\mathbf{y} = \{\phi_1, \phi_2, \dot{\phi}_1, \dot{\phi}_2\}^{\mathrm{T}}$. The coefficients in the nonlinear function $\mathbf{f}(\mathbf{y})$, which in our case is due to the cubic spring, are evaluated at critical values.

Considering u in an ε neighbourhood of u_c as $u = u_c + \varepsilon\mu$, by assuming that the eigenvalues of $\mathbf{A}$ have the general form $\lambda_{1,2} = \sigma_1 \pm i\omega_1$ and $\lambda_{3,4} = \sigma_2 \pm i\omega_2$, one can construct a modal matrix $\mathbf{P}$ enabling the system equations to be brought into the standard form

$$\dot{\mathbf{x}} = \Lambda\mathbf{x} + \varepsilon \mathbf{P}^{-1}\mathbf{f}(\mathbf{P}\mathbf{x}), \tag{33}$$

where

$$\mathbf{x} = \mathbf{P}^{-1}\mathbf{y}, \qquad \Lambda = \mathbf{P}^{-1}\mathbf{A}\mathbf{P} = \begin{bmatrix} \sigma_1 & -\omega_1 & 0 & 0 \\ \omega_1 & \sigma_1 & 0 & 0 \\ 0 & 0 & \sigma_2 & -\omega_2 \\ 0 & 0 & \omega_2 & \sigma_2 \end{bmatrix}. \tag{34}$$

6.1.1. *Hopf bifurcation*

At $u = u_c$ the first pair of eigenvalues becomes purely imaginary, $\lambda_{1,2} = \pm i\omega_0$, $\omega_0 > 0$, while $\lambda_{3,4} = -a \pm ib$, $a > 0$, $b > 0$. For ε sufficiently small, both σ_i and ω_i in (34) can be expanded in terms of ε:

$$\begin{aligned} \sigma_1 &= 0 + \varepsilon\mu_1 + \mathcal{O}(\varepsilon^2), & \omega_1 &= \omega_0 + \varepsilon\mu_3 + \mathcal{O}(\varepsilon^2), \\ \sigma_2 &= -a + \varepsilon\mu_2 + \mathcal{O}(\varepsilon^2), & \omega_2 &= b + \varepsilon\mu_4 + \mathcal{O}(\varepsilon^2). \end{aligned} \tag{35}$$

The coefficients μ_i, $i = 1, 2, 3, 4$, are the unfolding parameters, and they represent the effect of the deviation of the control parameter u from the critical value.

Let $\lambda = \sigma_1 \pm i\omega_1$ be the first pair of eigenvalues of $\mathbf{A}$, so that

$$\det[\mathbf{A} - (\sigma_1 \pm i\omega_1)\mathbf{I}] = R_1(\sigma_1, \omega_1, u) + iI_1(\sigma_1, \omega_1, u) = 0; \tag{36}$$

then we obtain for $u = u_c + \varepsilon\mu$ the following equations:

$$R_1(\varepsilon\mu_1, \omega_0 + \varepsilon\mu_3, u_c + \varepsilon\mu) = 0, \qquad I_1(\varepsilon\mu_1, \omega_0 + \varepsilon\mu_3, u_c + \varepsilon\mu) = 0. \tag{37}$$

Expanding R_1 and I_1 in terms of ε, and noting that $R_1(0, \omega_0, u_c)$ and $I_1(0, \omega_0, u_c) = 0$, results in

$$\varepsilon\mu_1 \frac{\partial R_1}{\partial \sigma_1} + \varepsilon\mu_3 \frac{\partial R_1}{\partial \omega_1} + \varepsilon\mu \frac{\partial R_1}{\partial u} = 0, \qquad \varepsilon\mu_1 \frac{\partial I_1}{\partial \sigma_1} + \varepsilon\mu_3 \frac{\partial I_1}{\partial \omega_1} + \varepsilon\mu \frac{\partial I_1}{\partial u} = 0, \tag{38}$$

where all derivatives are evaluated at the critical values.

As a special case, we took the case $h = 0{\cdot}5$ and $u = u_c = 2{\cdot}7396$, i.e. the velocity for which we obtained the first limit cycle, which corresponds to a Hopf bifurcation. Following the above calculation procedure, we obtained $\mu_1 = 31{\cdot}0465\mu$ and $\mu_3 = -19{\cdot}3943\mu$.

6.1.2. *Pitchfork bifurcation*

For a single zero eigenvalue, we let $\lambda = \sigma_2$ be the eigenvalue when $u = u_c + \varepsilon\mu$, and $\lambda = 0$ at $u = u_c = 1{\cdot}6946$; we thus have

$$\det(\mathbf{A} - \sigma_2 \mathbf{I}) = R_2(\sigma_2, u) = 0. \tag{39}$$

For ε small, letting $\sigma_2 = \varepsilon\mu_2$ at $u = 1{\cdot}6946 + \varepsilon\mu$, by expanding and evaluating $R_2(\sigma_2, u)$ we obtain

$$\varepsilon\mu_2 \frac{\partial R_2}{\partial \sigma_2}(0, u_c) + \varepsilon\mu \frac{\partial R_2}{\partial u}(0, u_c) = 0, \tag{40}$$

from which $\mu_2 = -4{\cdot}919\mu$.

6.2. Centre Manifold Calculations

6.2.1. *Hopf bifurcation*

For the critical flow velocity $u_c = 2{\cdot}7396$, the eigenvalues are $\lambda_{1,2} = \pm 9{\cdot}0176i$ (hence, $\sigma_1 = 0$, $\omega_1 = 9{\cdot}0176$) and $\lambda_{3,4} = -4{\cdot}4646 \pm 5{\cdot}2242i$ (hence, $\sigma_2 = -4{\cdot}4646$, $\omega_2 = 5{\cdot}2242$). The second of equations (34) may therefore be written as

$$\mathbf{\Lambda} = \begin{bmatrix} 0 & -9{\cdot}0176 & 0 & 0 \\ 9{\cdot}0176 & 0 & 0 & 0 \\ 0 & 0 & -4{\cdot}4646 & -5{\cdot}2242 \\ 0 & 0 & 5{\cdot}2242 & -4{\cdot}4646 \end{bmatrix}. \tag{41}$$

The system of equations (33) can be reduced to a two-dimensional system by centre manifold theory, involving the "centre space" of (41), i.e. the part associated with the purely imaginary eigenvalues; this leads to the reduced two-dimensional system

$$\begin{Bmatrix} \dot{x}_1 \\ \dot{x}_2 \end{Bmatrix} = \begin{bmatrix} \varepsilon\mu_1 & -(\omega_0 + \varepsilon\mu_3) \\ \omega_0 + \varepsilon\mu_3 & \varepsilon\mu_1 \end{bmatrix} \begin{Bmatrix} x_1 \\ x_2 \end{Bmatrix} + \{f(x_1, x_2)\}. \tag{42}$$

By replacing $\omega_0 = \omega_1 = 9{\cdot}0176$ and by substituting $\mu_1 = 31{\cdot}0465\mu$, $\mu_3 = -19{\cdot}3943\mu$,

as determined in Section 6.1.1, equation (42) gives

$$\begin{Bmatrix} \dot{x}_1 \\ \dot{x}_2 \end{Bmatrix} = \begin{bmatrix} 31{\cdot}0465\mu & -9{\cdot}0176 + 19{\cdot}3943\mu \\ 9{\cdot}0176 - 19{\cdot}3943\mu & 31{\cdot}0465\mu \end{bmatrix} \begin{Bmatrix} x_1 \\ x_2 \end{Bmatrix} + \{f(x_1, x_2)\}, \tag{43}$$

where

$$\{f(x_1, x_2)\} = \begin{Bmatrix} f_1 \\ f_2 \end{Bmatrix} = \begin{Bmatrix} 0{\cdot}1968x_1^3 - 1{\cdot}2342x_1^2x_2 + 2{\cdot}5775x_1x_2^2 - 1{\cdot}7943x_2^3 \\ 0{\cdot}9246x_1^3 - 5{\cdot}7989x_1^2x_2 + 12{\cdot}1102x_1x_2^2 - 8{\cdot}4301x_2^3 \end{Bmatrix}. \tag{44}$$

Either the method of normal forms or the method of averaging may be used to solve these equations. We shall use the latter and, accordingly, let

$$x_1 = r\cos\theta, \qquad x_2 = r\sin\theta. \tag{45}$$

Then, after substituting into (44) and applying the method, the averaged equations

$$\dot{r} = \varepsilon(\mu_1 + ar^2) + \mathcal{O}(\varepsilon^2), \qquad \dot{\theta} = \omega_0 + \varepsilon\mu_2 + ebr^2 + \mathcal{O}(\varepsilon^2) \tag{46}$$

are obtained, where

$$a = [f_{1,12} + 3f_{1,30} + 3f_{2,03} + f_{2,21}]/8. \tag{47}$$

The terms $f_{i,jk}$ are the coefficients of f_i $(i = 1, 2)$ in equation (44), in which jk is associated with $x_1^j x_2^k$ (Guckenheimer & Holmes 1983); for example, $f_{1,12} = 2{\cdot}5775$.

In the case under consideration, it is found that $a = -3{\cdot}4902$, i.e. $a < 0$, signifying that the Hopf bifurcation is supercritical (Guckenheimer & Holmes 1983). Limit-cycle motions are obtained when $\dot{r} = 0$, or from (46)

$$r^2 = -\mu_1/a = 8{\cdot}8954\mu. \tag{48}$$

It is seen that a real limit-cycle amplitude, r, exists only for $\mu \equiv u - u_c > 0$. For $\mu < 0$, the origin (undeformed equilibrium) is stable, and a limit cycle does not exist.

The phase plot in Figure 14(a) is for $u = 2{\cdot}73 < u_c$, where $u_c = 2{\cdot}7396$, i.e. for

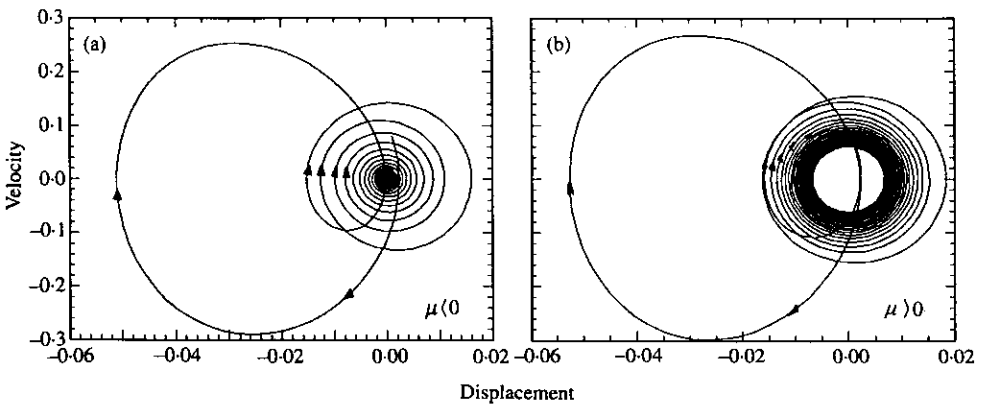

Figure 14. Analytical, centre-manifold representations of system behaviour ($h = 0{\cdot}5$, $\kappa_c = 5 \times 10^3$): (a) just before and (b) after the Hopf bifurcation.

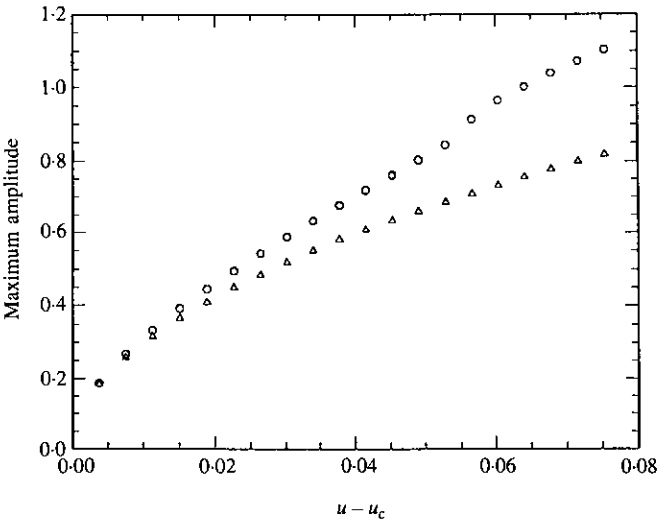

Figure 15. The post-Hopf limit-cycle amplitude versus $\mu \equiv u - u_c$ for the $h = 0{\cdot}5$ system with $\kappa_c = 5 \times 10^3$, as obtained numerically (Runge-Kutta) and analytically by centre-manifold reduction. ○, Runge–Kutta; △, centre manifold.

$\mu = -0{\cdot}0096 < 0$, where the origin is stable. If $u = 2{\cdot}74 > u_c$, then $\mu = 0{\cdot}0004 > 0$ and the origin becomes unstable; we then obtain a limit cycle, as seen on the phase plot in Figure 14(b).

We have also compared the maximum amplitude of the system as a function of μ, as obtained by (i) the centre manifold approximation and (ii) the Runge–Kutta numerical integration. Agreement between the two is very good for $\mu < 0{\cdot}02$, as can be seen in Figure 15; in terms of order of magnitude, it is quite acceptable up to $\mu \simeq 0{\cdot}08$. This gives a taste for the power of the centre manifold method, on the one hand, and gives confidence to the veracity of the numerical results, on the other.

6.2.2. *Pitchfork bifurcation*

For the same system, but for $u_c = 1{\cdot}6946$, the threshold flow velocity for pitchfork bifurcation, the matrix $\mathbf{\Lambda}$ is found to be

$$\mathbf{\Lambda} = \begin{bmatrix} -1{\cdot}8371 & -21{\cdot}5414 & 0 & 0 \\ 21{\cdot}5414 & -1{\cdot}8371 & 0 & 0 \\ 0 & 0 & 0 & 0 \\ 0 & 0 & 0 & -2{\cdot}4111 \end{bmatrix}. \tag{49}$$

Application of centre manifold theory in this case (see Section 6.1.2) reduces the full system into a one-dimensional sub-system,

$$\dot{x}_3 = \mu_2 x_3 - 11{\cdot}5757 x_3^3 = -(4{\cdot}919 \mu x_3 + 11{\cdot}5757 x_3^3), \tag{50}$$

where $\mu_2 = -4{\cdot}919\mu$, obtained in Section 6.1.2, has been utilized.

For $u = 1{\cdot}6 < u_c = 1{\cdot}6946$ (i.e., for $\mu < 0$), the origin is stable, as can be seen in the

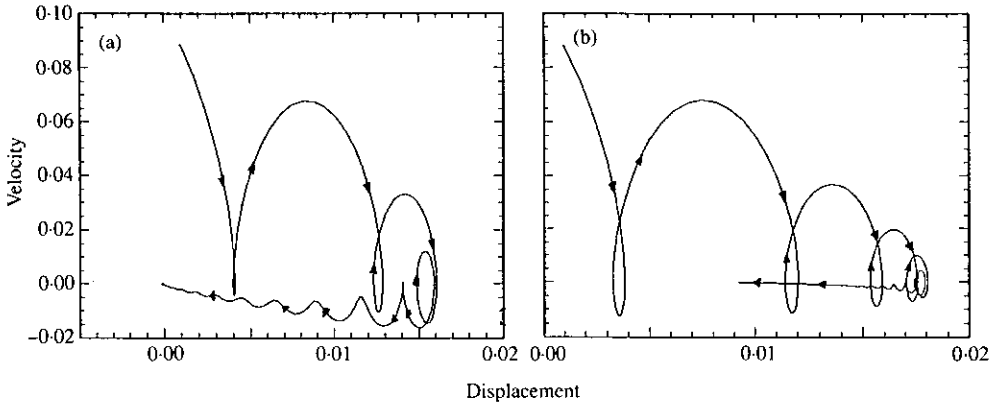

Figure 16. Analytical, centre-manifold representations of system behaviour of the $h = 0{\cdot}5$ system with $\kappa_c = 5 \times 10^3$, (a) just prior to and (b) just after divergence ($u_c = 1{\cdot}695$ for pitchfork bifurcation), showing: (a) that the origin (0, 0) is a stable fixed point, and (b) that the origin is no longer stable, but another fixed point (0·009, 0) has arisen.

phase plot in Figure 16(a); but for $\mu > 0$, e.g. $u = 1{\cdot}7$, the origin becomes unstable, as can be seen in Figure 16(b), where the trajectory ends at one of the new fixed points.

7. RESULTS FOR THREE-DEGREE-OF-FREEDOM SYSTEM

To avoid confusion, all the results for the three-degree-of-freedom system ($N = 3$) are presented in this section, paralleling the work for $N = 2$ presented in Sections 4 and 5.

The dimensionless equations of small motions in this case are as follows:

$$
\begin{aligned}
&[1+(\chi-1)\beta]\left[(\tfrac{4}{3}+e)\ddot{\phi}_1+(\tfrac{1}{2}+e)\ddot{\phi}_2+\frac{e^2}{2}\ddot{\phi}_3\right]+\chi\mu N\sqrt{\beta}\dot{\phi}_1\\
&\quad+\frac{3e+4}{6}\varepsilon c_f u\sqrt{\beta}\dot{\phi}_1+\frac{3e+4}{6}\varepsilon c\sqrt{\beta}\dot{\phi}_1+\frac{2e+1}{4}\varepsilon c_f u\sqrt{\beta}\dot{\phi}_2+2\chi uN\sqrt{\beta}\dot{\phi}_2\\
&\quad+\frac{2e+1}{4}\varepsilon c\sqrt{\beta}\dot{\phi}_2+\frac{e^2}{4}\varepsilon c_f u\sqrt{\beta}\dot{\phi}_3+2\chi uNe\sqrt{\beta}\dot{\phi}_3+\frac{e^2}{4}\varepsilon c\sqrt{\beta}\dot{\phi}_3-\chi uNf\sqrt{\beta}\dot{\phi}_1\\
&\quad-\chi u^2N^2f\phi_3-\chi fuN\sqrt{\beta}\dot{\phi}_2-\chi feuN\sqrt{\beta}\dot{\phi}_3-\chi u^2N^2(\phi_1-\phi_3)+2N^4\phi_1+N\gamma\frac{3+2e}{2}\phi_1\\
&\quad-N^4\phi_2+\frac{(1+h^{-1})(2e+3)}{4}u^2N\varepsilon c_f\phi_1+\frac{u^2N^2}{2}c_b\phi_1-\frac{u^2N^2}{2}c_b\phi_3=0,
\end{aligned}
\tag{51}
$$

$$
\begin{aligned}
&[1+(x-1)\beta]\left[(\tfrac{1}{2}+e)\ddot{\phi}_1+(\tfrac{1}{3}+e)\ddot{\phi}_2+\frac{e^2}{2}\ddot{\phi}_3\right]+\frac{1+2e}{4}\varepsilon c_f u\sqrt{\beta}\dot{\phi}_1\\
&\quad+\frac{1+2e}{4}\varepsilon c\sqrt{\beta}\dot{\phi}_1+\frac{3e+1}{6}\varepsilon c_f u\sqrt{\beta}\dot{\phi}_2+\frac{3e+1}{6}\varepsilon c\sqrt{\beta}\dot{\phi}_2-\chi uNf\sqrt{\beta}\dot{\phi}_1\\
&\quad+(1-f)\chi uN\sqrt{\beta}\dot{\phi}_2+\chi(2-f)euN\sqrt{\beta}\dot{\phi}_3+\tfrac{1}{4}\varepsilon c_f e^2u\sqrt{\beta}\dot{\phi}_3+\tfrac{1}{4}\varepsilon c\sqrt{\beta}e^2\dot{\phi}_3-\chi u^2N^2\phi_2\\
&\quad+2N^4\phi_2+N\gamma\frac{1+2e}{2}\phi_2-N^4(\phi_1+\phi_3)+\frac{(1+h^{-1})(2e+1)}{4}u^2N\varepsilon c_f\phi_2+\frac{u^2N^2}{2}c_b\phi_2\\
&\quad-\frac{u^2N^2}{2}c_b\phi_3+\chi(1-f)u^2N^2\phi_3=0,
\end{aligned}
\tag{52}
$$

$$[1+(\chi-1)\beta][\tfrac{1}{2}e^2\ddot{\phi}_1+\tfrac{1}{2}e^2\ddot{\phi}_2+\tfrac{1}{3}e^3\ddot{\phi}_3]+\frac{e^2}{4}\varepsilon c_f u\sqrt{\beta}\dot{\phi}_2+\frac{e^2}{4}ec\sqrt{\beta}\dot{\phi}_2$$
$$-\chi uNef\sqrt{\beta}\dot{\phi}_2+\tfrac{1}{6}e^3\varepsilon c_f u\sqrt{\beta}\dot{\phi}_3+\tfrac{1}{6}e^3\varepsilon c\sqrt{\beta}\dot{\phi}_3+\chi(1-f)uNe^2\sqrt{\beta}\dot{\phi}_3$$
$$+N^4(\phi_3-\phi_2)-\chi u^2N^2ef\phi_3+\frac{e^2}{4}(h^{-1}+1)u^2N\varepsilon c_f\phi_3+\frac{N\gamma}{2}e^2\phi_3+\frac{1}{4}\varepsilon c_f e^2u\sqrt{\beta}\dot{\phi}_1$$
$$+\tfrac{1}{4}\varepsilon c\sqrt{\beta}e^2\dot{\phi}_1-\chi efuN\sqrt{\beta}\dot{\phi}_1=0. \tag{53}$$

The same two cases are considered here as in the foregoing, with parameters as given by relations (28) and (29), but $N=3$: Case 1 ($h=0{\cdot}5$, $c=0{\cdot}38$) and Case 2 ($h=0{\cdot}2$, $c=0{\cdot}79$), the first corresponding to the wider annulus and the second to the narrower one. For convenience of presentation of the results, Case 2 is discussed first.

7.1. The Narrower Annulus System ($h=0{\cdot}2$, $c=0{\cdot}79$, $N=3$)

The dynamics of the linearized system of equations (51)–(53) is considered first, i.e. the dynamics for small-amplitude motions without impact with the outer channel.

The complex eigenvalues of the system are presented in Figure 17 in the form of Argand diagrams, as functions of the dimensionless flow velocity, u.

As u is increased, it is seen in Figure 17(a) that the first mode undergoes a pitchfork

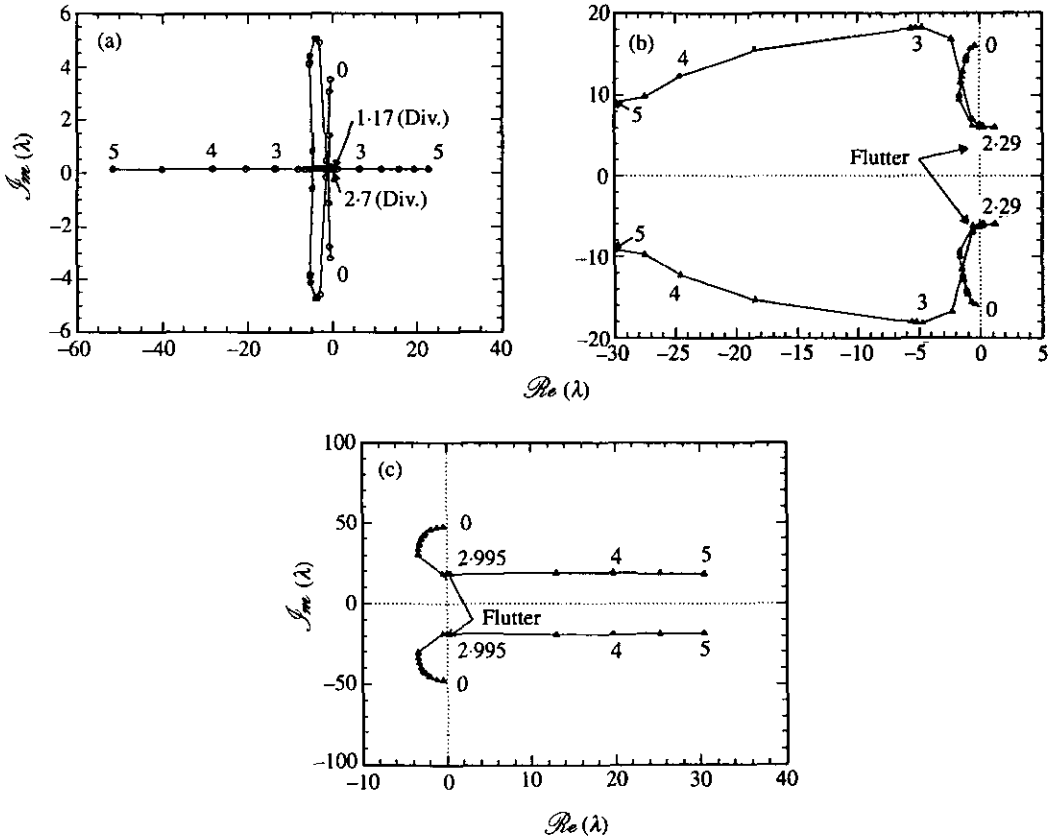

Figure 17. Argand diagrams for the three-degree-of-freedom system ($N=3$), for (a) first mode, (b) second mode, (c) third mode of the system of Case 2 ($h=0{\cdot}2$). The imaginary part of the eigenvalue, $\mathscr{I}m(\lambda)$, is plotted versus the real part, $\mathscr{R}e(\lambda)$, with the nondimensional flow velocity, u, as parameter.

bifurcation (divergence) at $u = 1{\cdot}1733$. As u is increased further, the system is restabilized in this mode at $u = 1{\cdot}9544$.

For $u = 2{\cdot}287$, purely imaginary eigenvalues arise in the second mode [Figure 17(b)], signalling a Hopf bifurcation (flutter). This dynamical state persists up to $u = 2{\cdot}6568$, at which point the system regains stability and remains stable in that mode thereafter. Then, for $u = 2{\cdot}6989$, the system undergoes a second pitchfork bifurcation [$u \simeq 2{\cdot}7$ in Figure 17(a)], and remains unstable in that mode to at least $u = 5$. At a slightly higher flow velocity ($u = 2{\cdot}995$), the system loses stability in its third-mode also, by another Hopf bifurcation, as seen in Figure 17(c). Thus, for $u \geq 2{\cdot}995$ and up to at least $u = 5$ the system is subject concurrently to divergence in its first mode and flutter in its third.

Next, the dynamics of the system with impacting is considered, modelled with the idealized cubic-spring representation of equation (31) and $\kappa_c = 5 \times 10^3$.

Figure 18 gives the bifurcation diagram in the range $2{\cdot}25 < u < 2{\cdot}85$; Figure 18(b) represents a blow-up of 18(a) for the higher values of u. The "maximum

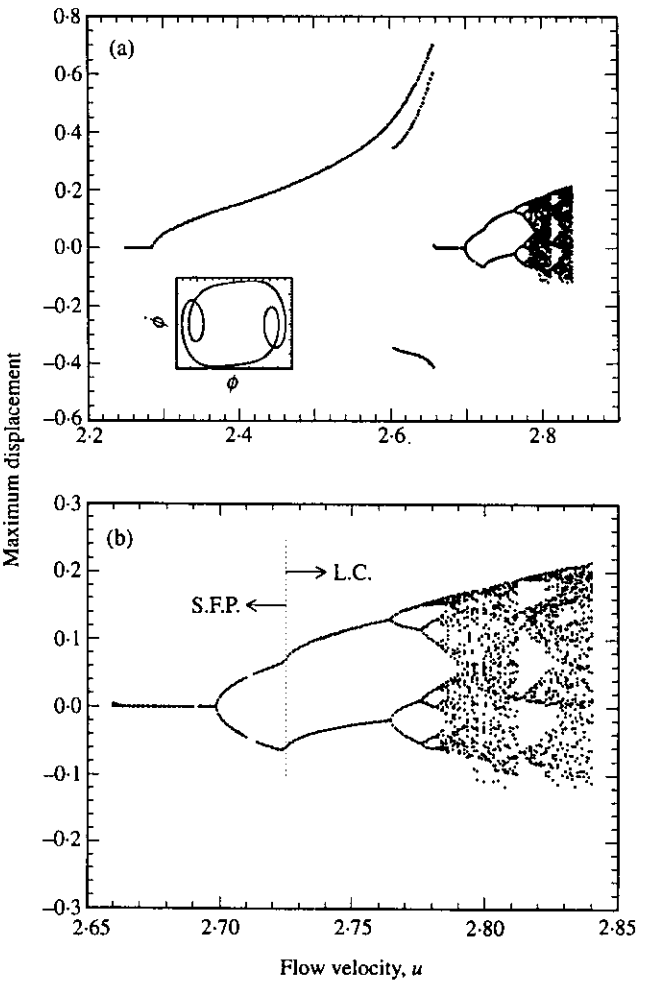

Figure 18. (a) Bifurcation diagram for the system with narrower annulus, $h = 0{\cdot}2$, $N = 3$ (Case 2), showing $\phi_{1\max}$ versus u, obtained with the cubic spring model for impacting with the channel ($\kappa_c = 5 \times 10^3$), and the phase plot for $u = 2{\cdot}568$. (b) Detailed bifurcation diagram for the same system, for $2{\cdot}65 < u < 2{\cdot}85$, showing the onset of chaos; S.F.P. stands for stable fixed point, while L.C. denotes limit-cycle motion.

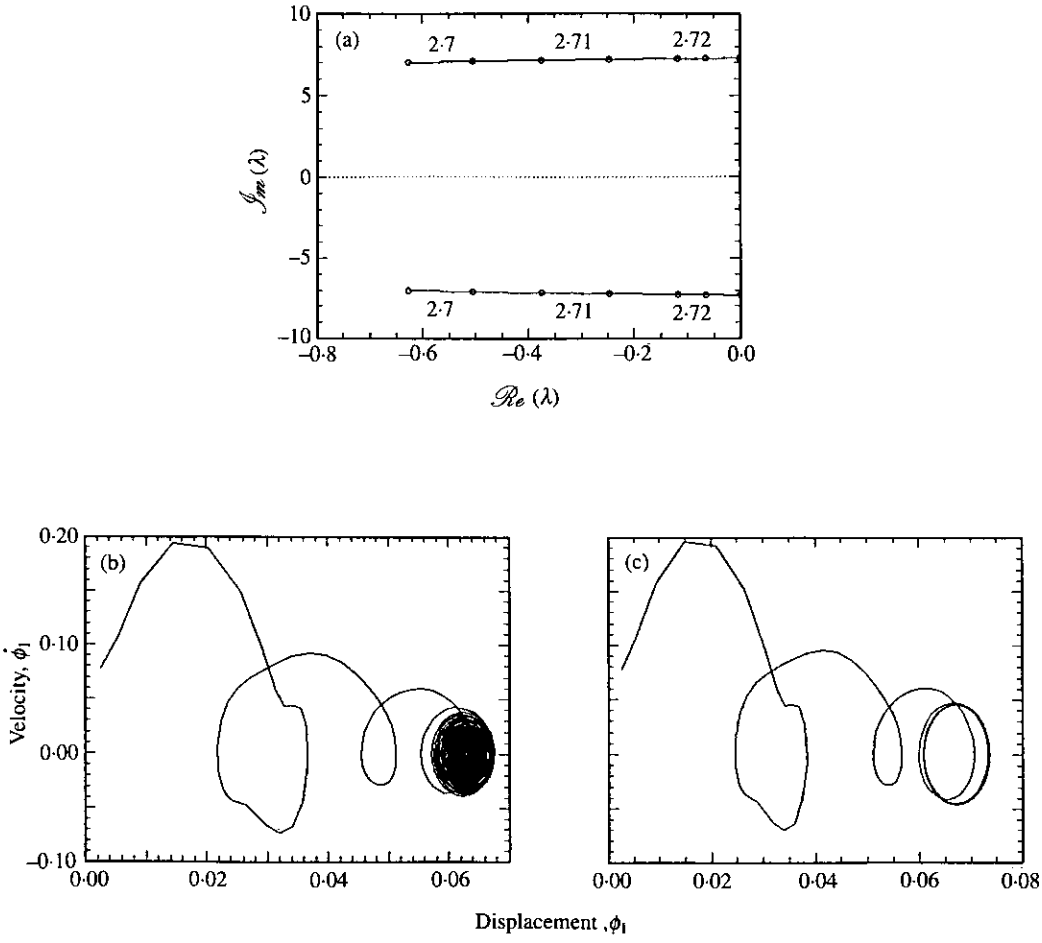

Figure 19. (a) Argand diagram for the second mode of the linearized system around the stable fixed points (S.F.P.) of Figure 18(b). (b) Phase-plane plot of $\dot{\phi}_1$ versus ϕ_1 for the system of Figure 18 ($h = 0{\cdot}2$, $N = 3$, $\kappa_c = 5 \times 10^3$) for $u = 2{\cdot}7225$, and (c) for $u = 2{\cdot}7250$; the trajectory in (b) ends at a stable fixed point, while (c) leads to a limit cycle.

displacement" corresponds to that of the first cylinder, $\phi_{1\max}$. Phase-plane plots and related information to clarify the behaviour depicted in the bifurcation diagram are presented in Figures 18 and 19.

The evolution of the limit-cycle amplitude beyond the first Hopf bifurcation is clearly seen on the left-hand side of Figure 18(a). For $2{\cdot}60 < u < 2{\cdot}66$ approximately, three values of amplitude are shown, corresponding to *local* maxima of $\phi_{1\max}$, as clarified by the inset phase-plane diagram: by taking a line close to $\dot{\phi} = 0$, three local maxima (two positive and one negative) are counted for ϕ, as well as three local minima.

At $u = 2{\cdot}6568$ the origin regains its stability and is a simple fixed point, up to $u \simeq 2{\cdot}70$, the threshold of the second divergence (pitchfork bifurcation), as best seen in Figure 18(b). The two branches of the pitchfork were determined via opposite-sign initial conditions. Thus, for $u > 2{\cdot}7$, the origin is no longer a stable fixed point, but new stable fixed points (S.F.P.) on either side are generated.

The stability of these new fixed points was investigated by linearizing the system in their vicinity. As seen in Figure 19(a), as u is increased (to $u = 2{\cdot}7225$) the eigenvalues become purely imaginary, at the extreme right of the figure, signifying the onset of

another Hopf bifurcation and the development of limit-cycle motions (L.C.) for higher u, the onset of which is marked by the kink in the curves in Figure 18(b). This is further clarified by the phase-plane plots of Figure 19(b, c). For $u = 2{\cdot}7225$ the fixed point is still stable and the trajectory of Figure 19(b) approaches that point with time. For $u = 2{\cdot}725$, however, which is beyond the Hopf bifurcation, a limit cycle develops, as seen in Figure 19(c). The limit cycle is symmetric about the fixed point which gave it birth, but asymmetric *vis-à-vis* the origin; only the upper (maximum) branch of the limit cycle is shown in the bifurcation diagram of Figure 18(b) for each of the two limit cycles—arising from one or the other of the two fixed points.

For $u > 2{\cdot}76$, a cascade of period-doubling bifurcations is seen in Figure 18(b), leading to chaos. Period-2, period-4 and period-8 motions are displayed in the corresponding phase portraits of Figure 20(b, c, d), respectively. The thresholds for period-2 to period-16 motion were pin-pointed as follows: $u = 2{\cdot}765$, $2{\cdot}7769$, $2{\cdot}782$ and $2{\cdot}7831$, from which a Feigenbaum number based on the last three is Fei = 4·64, close to the "ideal".

Figure 20(e), for $u = 2{\cdot}835$, shows chaotic motion. The corresponding Poincaré map displays an interesting "nebula" shape; it was obtained by plotting $\dot{\phi}_2$ versus ϕ_2 when $\phi_1 = 0$.

As discussed in conjunction with the eigenvalue analysis, interesting dynamical behaviour was expected to arise for $u > 2{\cdot}995$, when the system should be subject concurrently to (i) flutter associated with the third mode (via a Hopf bifurcation of the origin) and (ii) flutter associated with the first mode [via Hopf bifurcations of the new stable points emanating from the second pitchfork bifurcation shown in Figure 18(b)]. Unfortunately, no convergent solutions could be obtained for $u > 2{\cdot}84$ approximately; this was confirmed not to be a fault of the solution algorithm. The most likely cause is that the amplitudes of motion become too large, while the basic analytical model is for small amplitude motions.

7.2. The Wider Annulus System ($h = 0{\cdot}5$, $c = 0{\cdot}38$, $N = 3$)

The qualitative linear dynamics of small-amplitude motions is broadly the same as for the narrower annulus: a succession of divergence and flutter instabilities. In the interests of brevity, these results will not be presented. Instead, what is quite different, namely the route to chaos, will be focussed upon.

Figure 21 summarizes the results for (a) $u = 4{\cdot}0885$, (b) $u = 4{\cdot}0900$, and (c) $u = 4{\cdot}0965$: in the first column [panels (a_1), (b_1), (c_1)] are the phase-plane portraits, in the middle column the corresponding Poincaré maps, and in the last column the corresponding power spectra.

The nature of the dynamical states depicted in Figure 21 may best be assessed by the power spectra. In Figure $21(a_3)$, two fundamental frequencies are found: $f_1 = 0{\cdot}934\,4006$ and $f_7 = 6{\cdot}612\,681$, from which all other frequency peaks may be constructed, occurring at $nf_1 \pm mf_7$, where n and m are integers. Thus, these peaks occur at $f_n = nf_1$ for $n = 2, 3, \ldots, 9$, $f_{10} = 3f_1 + f_7$, $f_{11} = 4f_1 + f_7$, $f_{12} = 12f_1$, $f_{13} = 6f_1 + f_7$, $f_{14} = 14f_1$, $f_{15} = 2f_7$, $f_{16} = 15f_1$, $f_{17} = 9f_1 + f_7$, $f_{18} = 10f_1 + f_7$. Whether the ratio f_1/f_7 is rational or irrational depends on the accuracy of the determination of the frequencies f_1 and f_7. If one presumes that the values given here are absolutely precise, then, by the continued fraction technique and *Mathematica*, one finds a rational ratio $f_1/f_7 = 0{\cdot}1413044 = 13/92$. On the other hand, the "closed" nature of the curves depicted in the Poincaré map of Figure $21(a_2)$ suggests that this ratio may be irrational after all.

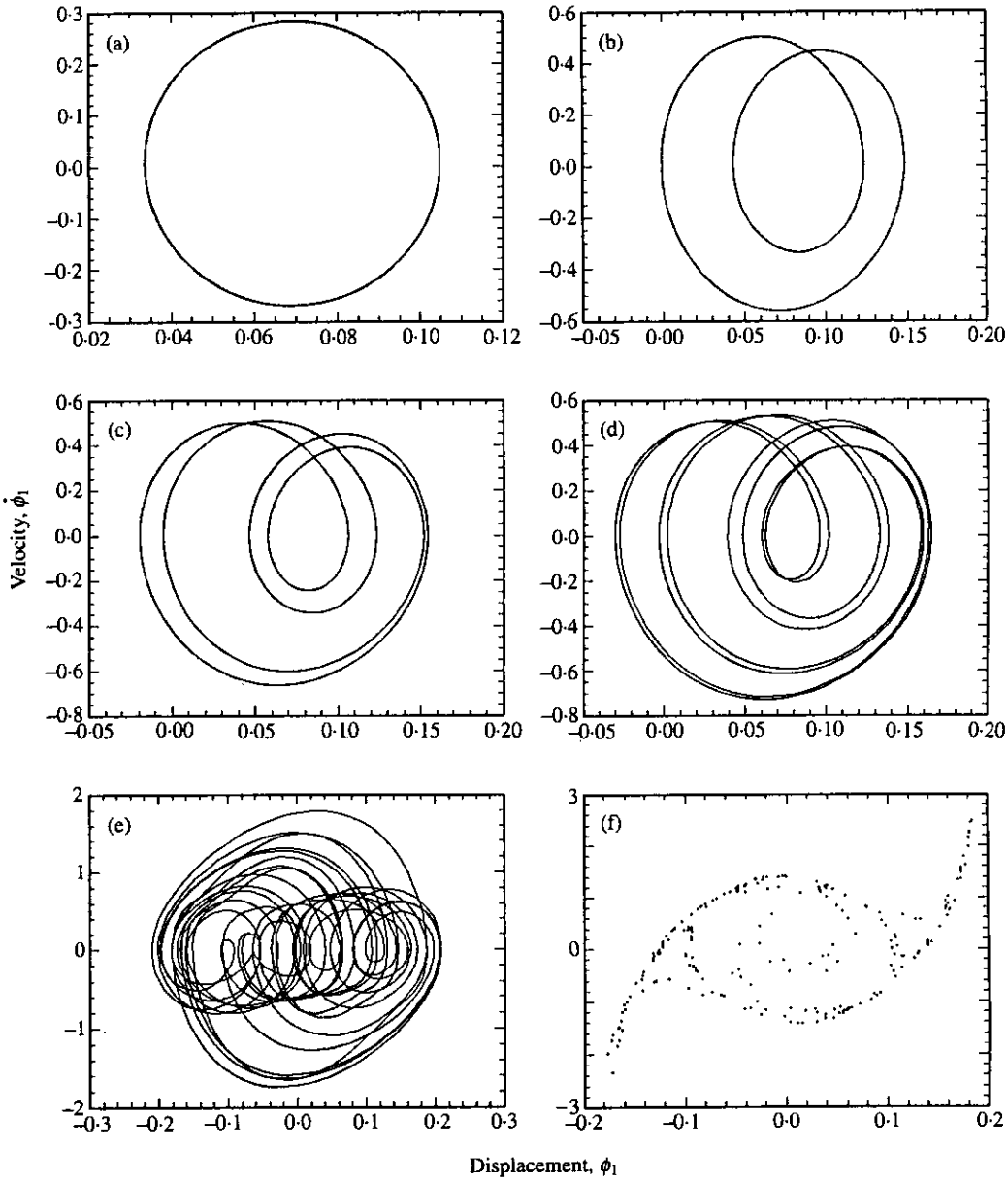

Figure 20. Phase-plane plots of $\dot{\phi}_1$ versus ϕ_1 at (a) $u = 2{\cdot}74$, (b) $u = 2{\cdot}77$, (c) $u = 2{\cdot}778$, (d) $u = 2{\cdot}7825$, (e) $u = 2{\cdot}835$, for the system of Figure 18 (Case 2: $h = 0{\cdot}2$, $N = 3$, $\kappa_c = 5 \times 10^3$); (f) Poincaré map of $\dot{\phi}_2(\tau)$ versus $\phi_2(\tau)$ when $\phi_1(\tau) = 0$ for $u = 2{\cdot}835$.

The important point is that the motion, as it involves two fundamental frequencies, is quasiperiodic-two.

The power spectrum for Figure 21(b_3) is found to involve three fundamental frequencies, $f_1 = 0{\cdot}8625236$, $f_2 = \frac{5}{4}f_1$ and $f_5 = \frac{10}{3}f_1$; hence the motion is quasiperiodic-three in this case. All other frequencies may be constructed by $nf_1 \pm mf_2 \pm pf_5$, with n, m, and p being integers. Thus, for example, $f_3 = 2f_1$, $f_4 = f_1 + f_2$, $f_6 = f_1 + f_5$, $f_7 = 2f_1 + f_5$, $f_8 = f_1 + f_2 + f_5$, $f_9 = 2f_1 + f_2 + f_5$, $f_{10} = 3f_1 + f_2 + f_5$, $f_{11} = 12f_1 - f_5$, and so on. In this case, the ratios of the fundamental frequencies are definitely rational ($\frac{5}{4}$ and $\frac{10}{3}$), which is

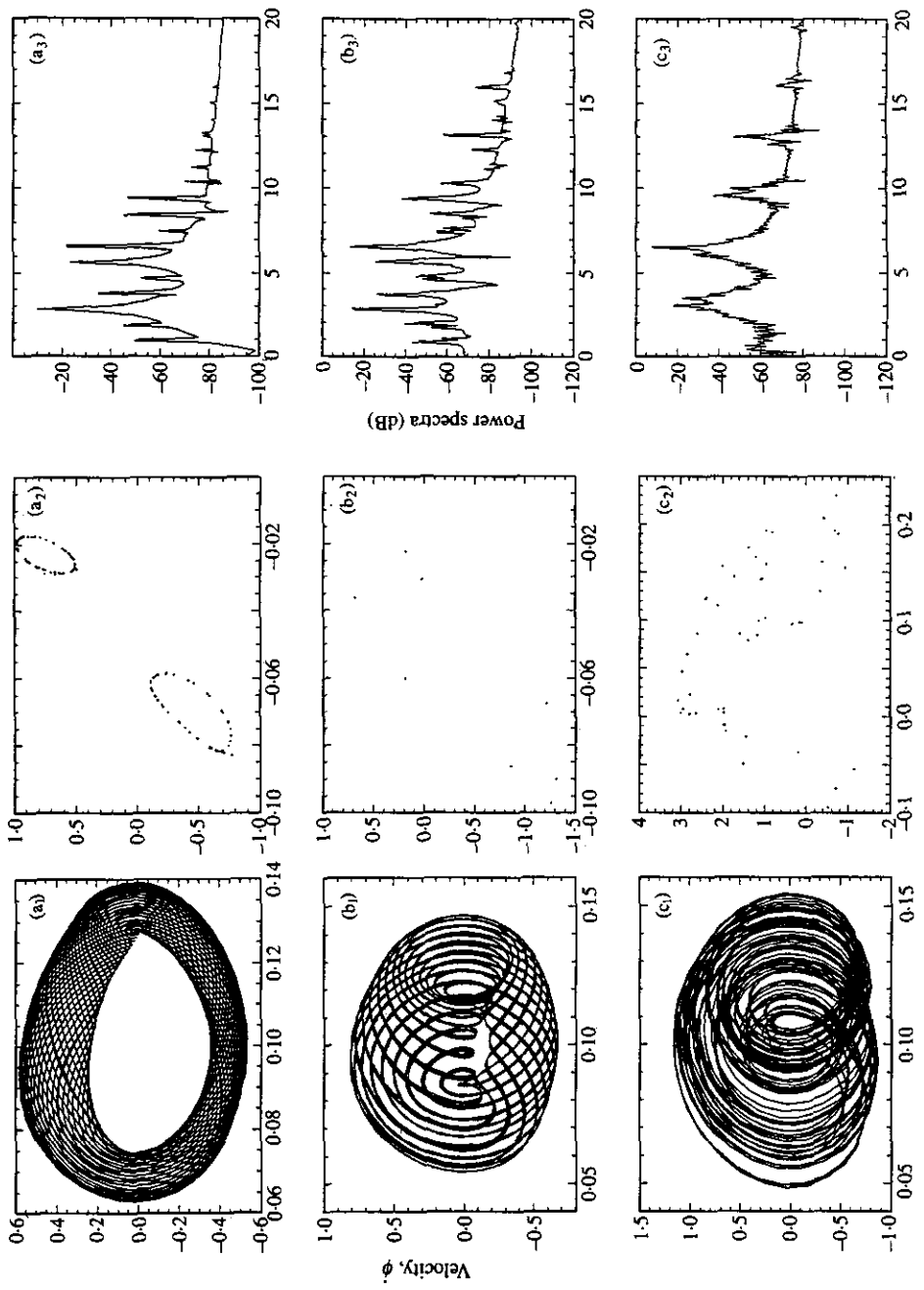

Figure 21. Phase-plane plots (first column), Poincaré maps (second column) and power spectra (third column) for the three-degree-of-freedom, wider annulus system (Case 1: $h = 0{\cdot}5$, $N = 3$, $\kappa_c = 5 \times 10^3$), for (a) $u = 4{\cdot}0885$, (b) $u = 4{\cdot}0900$ and (c) $u = 4{\cdot}0965$.

supported by the relatively small number of points associated with the Poincaré map of Figure 21(b_2). In this connection, it ought to be remarked that the precise number of points in the Poincaré map depends on the section one takes. Figure 21(b_2), with nine points, was obtained by plotting $\dot{\phi}_2$ versus ϕ_2 when $\phi_1 = 0{\cdot}1$; if the condition is altered to $\phi_1 = 0{\cdot}12$, for example, then one obtains 16 points.

The system for $u = 4{\cdot}0965$ is clearly chaotic, as evidenced by the phase portrait of Figure 21(c_1) and the power spectrum of Figure 21(c_3). In the latter, although the principal frequencies (twin peak) and their harmonics are still very prominent, the subharmonic content is fundamentally flat.

The route to chaos may be explained by means of the Ruelle–Takens–Newhouse theory (Ruelle & Takens 1971; Bergé *et al.* 1984), the overall process involving three successive Hopf bifurcations. The first leads from an initial steady static state (fixed point, dimension zero) to a periodic one (limit cycle, dimension one). The second transforms the periodic regime into a quasiperiodic-two regime [Figure 21(a)]. The third gives a transition to quasiperiodic-three motions [Figure 21(b)], which finally gives rise to chaos [Figure 21(c)].

8. CONCLUSIONS

In this paper, two- and three-degree-of-freedom articulated cylindrical systems subject to axisymmetrically confined axial flow have been considered. Motions of the system are assumed to be planar and the impacting of the cylindrical system with the external flow-confining cylindrical channel is modelled by a nonlinear trilinear or cubic spring; most of the calculations in this paper have been conducted with the cubic spring representation. The calculations presented, in the interests of brevity, are for two systems: Case 1 for a wider annulus ($h = 0{\cdot}5$) and Case 2 for a narrower one ($h = 0{\cdot}2$) with either two or three articulations (or number of cylinders) in the system, $N = 2$ or $N = 3$, which display different kinds of dynamical behaviour. It is shown, for the first time, that such a system can develop chaotic oscillations.

The first part of the nonlinear study, which generally follows an eigenvalue analysis of the linearized system, is numerical. The existence of chaotic vibrations, through impacting with the channel, has been proven and illustrated by the use of phase-plane portraits, bifurcation diagrams and power spectra, and through the construction of Poincaré maps and the computation of the Lyapunov exponents of the system.

For Case 1 ($h = 0{\cdot}5$) with $N = 2$, the route to chaos is via the classical cascade of period-doubling bifurcations, which occurs after a symmetry-breaking pitchfork bifurcation. Once it occurs, chaos persists over a wide range of flow velocities, interspersed by periodic windows. This being a very well documented dynamical behaviour, no more will be said about it.

Case 1 with $N = 3$ is fundamentally different. The route to chaos in this case is via the quasiperiodic route, following the classical Ruelle–Takens–Newhouse process: from period-1 to quasiperiodic-two (two fundamental frequencies), to quasiperiodic-three, and finally chaos.

Case 2 ($h = 0{\cdot}2$) with $N = 2$ is also unusual. Firstly, after the pitchfork bifurcation, the phenomenon of "period bubbling" takes place, where the forward period-doubling cascade (to period-2 in this case) is immediately followed by the inverse cascade, back to period-1. Secondly, chaos arises via the quasiperiodic route, involving only quasiperiodic-two motion; the quasiperiodic-three state of the Ruelle–Takens–Newhouse process has not been found—but this is not unusual (Bergé *et al.* 1984). Finally, Case 2 with $N = 3$ displays a number of unusual and interesting features, as

described in Section 7. The route to chaos in this case is via a cascade of period-doubling bifurcations, similar to that of Case 1 with $N = 2$.

Certain features of the dynamical behaviour for $N = 2$ and the narrow annulus are similar to those for $N = 3$ and the wider annulus; correspondingly, similarities were found between the $N = 2$ wide-annulus and the $N = 3$ narrow-annulus systems. This is fortuitous. The results for $N = 4$, which have not been presented in this paper, are much more similar to those of $N = 3$ for both values of h (narrow and wide annulus), showing the beginnings of convergence.† In fact, the dissimilarity in the results for $N = 2$ and $N = 3$ is not surprising if one compares with the work of Païdoussis & Deksnis (1970) for the analogous system involving an articulated system with internal flow; in that case also, where calculations for each N from 2 to 8 as well as for the continuously flexible system were conducted, the dynamics for $N = 2$ were particular, but $N = 3$ began to display generic behaviour, typical of higher values of N.

The second part of the nonlinear study is analytical, but is confined to $N = 2$ in this paper. Centre manifold theory is used, whereby the fourth-order system is reduced to one of second order (for the Hopf bifurcation) or first order (for the pitchfork bifurcation). The analytical results obtained fully support the numerical ones and demonstrate the usefulness and power of centre manifold theory.

The work and especially the results presented in this paper represent a sample of a larger set. In effect, the only parameter that was varied here, other than the flow velocity and the number of articulations, was the narrowness of the annulus [h and the corresponding c in relations (28) and (29)]; however, there are seven other system parameters in (28). The purpose was to demonstrate that this system is capable of displaying an extremely rich dynamical behaviour, and hence—especially as it corresponds to an interesting and practically important physical system—that it is deserving of further study.

ACKNOWLEDGEMENTS

The authors gratefully acknowledge the support by NSERC of Canada and FCAR of Québec which has made this research possible.

REFERENCES

BERGÉ, P., POMEAU, Y. & VIDAL, C. 1984 *Order within Chaos.* Paris: Hermann and New York: John Wiley.

BENETTIN, G., GALGANI, L., GIOGILLI, A., & STRELCYN, J. M. 1980 Lyapunov characteristic exponents for smooth dynamical systems and for Hamiltonian systems. A method for computing all of them. Part 2: numerical application. *Meccanica* **15,** 21–30.

BENJAMIN, T. B. 1961 Dynamics of a system of articulated pipes conveying fluid. *Proceedings of the Royal Society (London)* **261** (A), 457–499.

DOWLING, A. P. 1988a The dynamics of towed flexible cylinders. Part 1: neutrally buoyant elements. *Journal of Fluid Mechanics* **187,** 507–532.

DOWLING, A. P. 1988b The dynamics of towed flexible cylinders. Part 2: negatively buoyant. *Journal of Fluid Mechanics* **187,** 533–571.

GORMAN, D. J. 1971 An analytical and experimental investigation of the vibration of cylindrical reactor fuel elements in two-phase parallel flow. *Nuclear Science and Engineering* **44,** 277–290.

† Thus, for the case of $h = 0{\cdot}2$, the linear behaviour is quite similar: the first pitchfork bifurcation occurs at $u = 1{\cdot}17$ for both $N = 3$ and $N = 4$, the first Hopf bifurcation at $u = 2{\cdot}3$ and $2{\cdot}4$, respectively, for $N = 3$ and $N = 4$, and so on. Also, the nonlinear behaviour (with impacting), as shown by the bifurcation diagrams and the corresponding phase plots, is qualitatively similar (at least in the range $2{\cdot}3 < u < 2{\cdot}7$ for $N = 3$ and $2{\cdot}4 < u < 2{\cdot}8$ for $N = 4$).

GUCKENHEIMER, J. & HOLMES, P. J. 1983 *Nonlinear Oscillations, Dynamical Systems and Bifurcations of Vector Fields.* New York: Springer.

HAMY, N. 1971 *The Trebon Sea Chain System.* Trebon Holdings Ltd, Montreal, Canada.

HAWTHORNE, W. R. 1961 The early development of the Dracone flexible barge. *Proceedings of the Institution of Mechanical Engineers* (*London*) **175,** 52–83.

HENNIG, K., PLATEN, E. & GRUNWALD, G. 1980 Treatment of flow-induced pendulum oscillations. In *Practical Experiences with Flow-Induced Vibrations* (eds E. Naudascher and D. Rockwell), pp. 140–143. Berlin: Springer-Verlag.

LIGHTHILL, M. J. 1960 Note on the swimming of slender fish. *Journal of Fluid Mechanics* **9,** 305–317.

MATEESCU, D. & PAÏDOUSSIS, M. P. 1987 Unsteady viscous effects on the annular-flow-induced instabilities of a rigid cylindrical body in a narrow duct. *Journal of Fluids and Structures* **1,** 197–215.

MOON, F. C. 1987 *Chaotic Vibrations: An Introduction for Applied Scientists and Engineers.* New York: John Wiley & Sons.

PAÏDOUSSIS, M. P. 1966a Vibration of flexible cylinders with supported ends, induced by axial flow. *Proceedings Institution of Mechanical Engineers* **180,** 268–278.

PAÏDOUSSIS, M. P. 1966b Dynamics of flexible slender cylinders in axial flow. Part I: theory. *Journal of Fluid Mechanics* **26,** 717–736.

PAÏDOUSSIS, M. P. 1966c Dynamics of flexible slender cylinders in axial flow. Part II: experiments. *Journal of Fluid Mechanics* **26,** 737–751.

PAÏDOUSSIS, M. P. 1968 Stability of towed, totally submerged flexible cylinders. *Journal of Fluid Mechanics* **34,** 273–297.

PAÏDOUSSIS, M. P. 1973 Dynamics of cylindrical structures subjected to axial flow. *Journal of Sound and Vibration* **29,** 365–385.

PAÏDOUSSIS, M. P. 1976 Dynamics of fuel strings in axial flow. *Annals of Nuclear Energy* **3,** 19–30.

PAÏDOUSSIS, M. P. 1979 The dynamics of clusters of flexible cylinders in axial flow: theory and experiments. *Journal of Sound and Vibration* **65,** 391–417.

PAÏDOUSSIS, M. P. 1986 Stability of a chain of cylinders travelling underwater. *Proceedings of the Fifth International Offshore Mechanics and Arctic Engineering Symposium* **1,** pp. 483–490. New York: ASME.

PAÏDOUSSIS, M. P., CUSUMANO, J. P. & COPELAND, G. S. 1992 Low-dimensional chaos in a flexible tube conveying fluid. *Journal of Applied Mechanics* **59,** 196–205.

PAÏDOUSSIS, M. P. & DEKSNIS, E. B. 1970 Articulated models of cantilevers conveying fluid: the study of a paradox. *I. Mech. E. Journal of Mechanical Engineering Science* **12,** 288–300.

PAÏDOUSSIS, M. P., LI, G. X. & RAND, R. H. 1991 Chaotic motions of a constrained pipe conveying fluid: comparison between simulation, analysis and experiments. *Journal of Applied Mechanics* **58,** 559–565.

PAÏDOUSSIS, M. P., MATEESCU, D. & SIM, W.-G. 1990 Dynamics and stability of a flexible cylinder in a narrow coaxial cylindrical duct subjected to annular flow. *Journal of Applied Mechanics* **57,** 232–240.

PAÏDOUSSIS, M. P. & MOON, F. C. 1988 Nonlinear and chaotic fluidelastic vibrations of a flexible pipe conveying fluid. *Journal of Fluids and Structures* **2,** 567–591.

PETERKA, F. 1991 Flow-induced-impact oscillation of a spherical pendulum. *Journal of Fluids and Structures* **5,** 627–650.

REAVIS, J. R. 1969 Vibration correlation for maximum fuel-element displacement in parallel turbulent flow. *Nuclear Science and Engineering* **38,** 63–69.

RUELLE, D. & TAKENS, F. 1971 On the nature of turbulence. *Communications in Mathematical Physics* **20,** 167.

TAYLOR, G. I. 1952 Analysis of the swimming of long and narrow animals. *Proceedings of the Royal Society* (*London*) **214** (A), 158–183.